Dynamic control of hippocampal spatial coding resolution by local visual cues

Romain Bourboulou[1*], Geoffrey Marti[1*], François-Xavier Michon[1], Morgane Nouguier[1], David Robbe[1], Julie Koenig[1&] and Jérôme Epsztein[1&]

[1]Institute of Neurobiology of the Mediterranean Sea (INMED), French National Institute for Health and Research (INSERM UMRS1249), Aix-Marseille University, Marseille, France.

* Equally contributing first authors
& Co-senior authors
Correspondence
Drs Jérôme Epsztein or Julie Koenig
INMED/INSERM U1249
Parc scientifique de Luminy
163 route de Luminy
BP 13 13273
Marseille cedex 09
Tel: 00 33 4 91 82 81 47
jerome.epsztein@inserm.fr
julie.koenig@inserm.fr

1 Abstract

2 The ability to flexibly navigate an environment relies on a hippocampal-dependent internal

3 cognitive map. Explored space can be internally mapped at different spatial resolutions.

4 However, whether hippocampal spatial coding resolution can be dynamically controlled

5 within and between environments is unknown. In this work we recorded the firing of

6 hippocampal principal cells in mice navigating virtual reality environments, which differed by

7 the presence of local visual cues (virtual 3D objects). Objects improved spatial coding

8 resolution globally with a higher proportion of place cells, smaller place fields, increased

9 spatial selectivity and stability. Spatial coding resolution was notably enhanced locally near

10 objects and could be rapidly tuned by their manipulations. In the presence of objects, place

11 cells also displayed improved theta phase precession and theta timescale spike coordination.

12 These results suggest that local visual cues can rapidly tune the resolution of the

13 hippocampal mapping system within and between environments.

Introduction

14

15   Animals can flexibly navigate their environment. In mammals such as rodents and humans,

16   this ability is thought to rely on an internal cognitive map (Tolman, 1948; O'Keefe and Nadel,

17   1978; Epstein et al., 2017). When animals move in their environment, hippocampal place

18   cells fire in specific locations (their place fields) and this spatial tuning is believed to provide

19   a neuronal substrate to the cognitive map. To be useful for navigation, such internal

20   representation should be properly oriented and positioned in reference to the external

21   world. Distal visual cues or intramaze objects located at the border of an environment play a

22   predominant role in map orientation while environmental boundaries are important for map

23   anchoring (O'Keefe and Burgess, 1996; Knierim and Rao, 2003; Knierim and Hamilton, 2011).

24   A dynamic control of hippocampal spatial coding resolution between environments or

25   different regions of the same environment could be important for spatial navigation (Geva-

26   Sagiv et al., 2015). Spatial coding resolution can be improved by increasing the proportion of

27   spatially selective cells (place cells) coding for these locations (e.g. overrepresentation), by

28   reducing place field size but also by enhancing their spatial selectivity, stability and spatial

29   information content. Wild animals, including rodents, often travel kilometers away from

30   their home through empty space to specific food locations (Taylor, 1978). Mapping all

31   traveled space at similar spatial resolution would require a huge neuronal and

32   computational investment. Alternatively, mapping different parts of an environment at

33   different spatial resolutions could be advantageous. Previous studies have reported

34   increased place field density near rewarded locations (O'Keefe and Conway, 1978; Hollup et

35   al., 2001; Dupret et al., 2010; Danielson et al., 2016; Sato et al., 2018), salient sensory cues

36   (Wiener et al., 1989; Hetherington and Shapiro, 1997; Sato et al., 2018) or connecting parts

37   in multi-compartment environments (Spiers et al., 2015). Whether these

38   overrepresentations correspond to position coding at higher spatial resolution (i.e. the

39   resolution of the "where" information) or the coding of nonspatial information associated

40   with these particular locations (also referred to as "what" information) is difficult to

41   disentangle. If they would represent increased spatial resolution, then place fields should

42   not only be more numerous but they should also more accurately code for space in terms of

43   spatial selectivity, spatial information content and stability. Furthermore, in the context of

44   navigation, spatial coding resolution should be rapidly adjustable within and between

45 environments. Finally, improved spatial coding resolution should extend to the temporal

46 coding domain.

47   The factors controlling spatial coding resolution are poorly understood. Local sensory

48 cues, with a higher sensory resolution compared to distal cues, could be instrumental in this

49 process according to sensory-based models of place cell activation (O'Keefe and Burgess,

50 1996; Hartley et al., 2000; Barry et al., 2006; Geva-Sagiv et al., 2015; Strösslin et al., 2005;

51 Sheynikhovich et al., 2009). Here we took advantage of virtual reality (Holscher, 2005;

52 Youngstrom and Strowbridge, 2012; Chen et al., 2013; Ravassard et al., 2013; Aronov and

53 Tank, 2014; Cohen et al., 2017) to specifically control and manipulate local sensory cues and

54 test their impact on hippocampal spatial coding resolution. We recorded a large number of

55 hippocampal cells in area CA1 to be able to use decoding strategies to decipher the

56 functional impact of the changes observed. Our results show that local visual cues (virtual 3D

57 objects) increased spatial coding resolution globally with a higher proportion of place cells,

58 improved spatial selectivity, information content and stability. Spatial coding resolution was

59 notably enhanced near objects with a higher local density of place fields but also decreased

60 place field size and stability. Spatial resolution could be instantaneously tuned upon removal

61 or addition of local cues. Importantly, increased spatial coding resolution extended to the

62 temporal coding domain. Altogether our results suggest that the hippocampal system can

63 rapidly and dynamically adjust its spatial coding resolution within and between
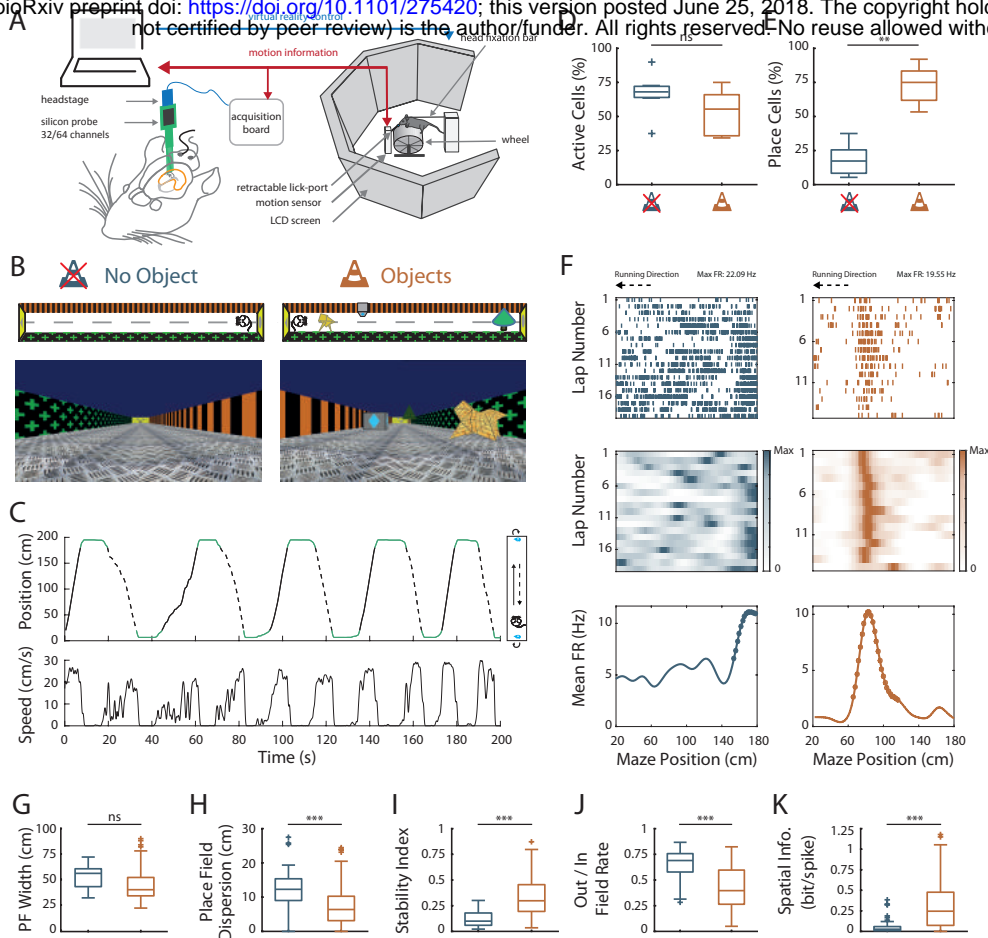
64 environments.

Results

Effects of local visual cues on spatial coding resolution

Head-fixed mice were trained to run on a wheel and to shuttle back and forth on a 2 m-long virtual linear track to collect liquid rewards at its extremities (Fig. 1A). The lateral walls of the virtual track displayed distinct visual patterns to provide directional information. However, these patterns did not provide any information relative to the position of the animal on track. To investigate the contribution of local cues to hippocampal spatial representation, mice were trained either in the presence or absence of 3D visual cues (hereafter called virtual objects; Object Track, OT: n = 2 mice; No Object Track, ØT: n = 3 mice), which were virtually positioned on the floor of the track between the animal trajectory and the walls (Fig. 1B). The running wheel forced the animals to run in a unidirectional manner so that they repetitively ran along the virtual objects without the possibility to orient toward them or explore them with any sensory modality but vision. Animals received a reward (sucrose in water 5%) each time they reached one of the extremities of the linear track. After licking, the mice were "teleported" in the same position but facing the opposite direction of the track (Fig. 1C), allowing them to run back and forth in the same environment. Once animals reached a stable and proficient behavior (at least 1 reward/minute during a 60 min-long session), we recorded spiking activity in the pyramidal cell layer of the CA1 hippocampal region using either 4-shanks or 8-shanks silicon probes (Fig. 1A, Figure 1-figure supplement 1) in the right and/or left hemispheres over the course of 2-3 days. A total of 1124 neurons were recorded in the CA1 pyramidal cell layer. Mice trained in ØT (n = 9 recording sessions) performed the task with similar proficiency than mice trained in OT (n = 5 recording sessions), as shown by similar rate of reward collections (ØT: 1.70 ± 0.29 rewards/minute, n = 9 recording sessions in 3 mice; OT: 1.15 ± 0.09 rewards/minute, n = 5 recording sessions in 2 mice; t_{12} = 1.40, P = 0.19, two-tailed unpaired t-test; all values expressed as mean ± SEM) and average running speed (ØT: 14.1 ± 2.12 cm/s, n = 9 recording sessions in 3 mice; OT: 16.8 ± 1.58 cm/s, n = 5 recording sessions in 2 mice; Z = -1.27, P = 0.24, two-tailed Wilcoxon rank sum (WRS) test; Fig. 1C).

To examine how local visual cues impacted spatial representation of the linear track we first compared the number of track-active putative pyramidal cells to assess for overall excitability and the proportion of place cells among them to assess for spatial resolution. The

5

96 percentage of track active cells was comparable in between the track without and with

97 virtual objects (ØT: 66.4 ± 5.8%, n = 7 sessions in 3 mice; OT: 52.8 ± 7.8%, n = 5 sessions in 2

98 mice; t_{10} = 1.43, P = 0.18, two-tailed unpaired t-test; Fig. 1D). However, while only 19% of

99 track active cells had at least one place field (place cells) in the empty track (n = 48 place

100 cells), 73% of track active cells were place cells when virtual objects were present (n = 103

101 place cells; t_{10} = -7.2, $P < 10^{-4}$, two-tailed unpaired t-test; Fig. 1E). In ØT, place fields were

102 relatively sparse in the middle of the track with a large proportion of them aligned either to

103 the beginning or to the end of the track (End-Track fields: 49.3 ± 8.99%, n = 7 sessions in 3

104 mice; Fig. 2A). In the maze with objects, however, the majority of fields was located in the

105 central part of the track (On-Track fields: 84.3 ± 1.50%; n = 5 sessions in 2 mice; Z = 2.03, P =

106 0.048, two-tailed WRS test; Fig. 2A). These results indicate that local visual cues can strongly

107 increase the proportion of place cells among active cells notably to code the central part of

108 the maze.

109   Another factor influencing spatial resolution is place field size. There was a tendency

110 for place field width (calculated on complete fields) to be lower in the track with objects (ØT:

111 51.5 ± 3.33 cm, n = 15 place fields; OT: 44.6 ± 1.60 cm, n = 95 place fields; Z = 1.92, P = 0.055,

112 two-tailed WRS test; Fig. 1G), in agreement with a higher spatial coding resolution.

113 Decreased place field width could be due to spatial shrinking of place fields detected on a

114 trial-by-trial basis, could result from decreased inter-trial variability in their position, or both.

115 To decipher among these possibilities, we detected place fields on single trials then

116 calculated their size and averaged them to get a single value for each place field(Cabral et

117 al., 2014). The size of place fields based on single trial detection was not significantly

118 different between the two conditions (ØT: 34.4 ± 1.2 cm, n = 15 place fields; OT: 33.5 ± 0.6

119 cm, n = 94 place fields; Z = 1.1, P = 0.28, two-tailed WRS test). On the other hand, the spatial

120 dispersion of single-trial detected place fields was significantly reduced in the presence of 3D

121 objects (ØT: 11.9 ± 0.90 cm, n = 48 place cells; OT: 7.58 ± 0.55 cm, n = 103 place cells; Z =

122 4.25, $P < 10^{-4}$, two-tailed WRS test; Fig. 1H). These results suggest that the decreased place

123 field size resulted from decreased inter-trial spatial dispersion. To further assess inter-trial

124 place field stability, independently from place field detection, we calculated a stability index

125 (based on spatial correlations between all pairs of firing rate vectors, see Materials and

126 methods section). This stability index was significantly lower in the track without objects

127 (ØT: 0.12 ± 0.01, n = 48 place cells; OT: 0.34 ± 0.02, n = 103 place cells; Z = -7.26, $P < 10^{-12}$,

6

Figure 1: Effects of virtual 3D objects on spatial coding resolution

A. Schema of the virtual reality set up. The mouse is head-fixed and located on a wheel surrounded by LCD screens where a virtual environment is displayed. **B.** Top and first person views of virtual linear tracks used. Left: track without objects (ØT) and right: track with virtual 3D objects (OT). **C.** Top: Animal's position in the virtual track as a function of time. Green lines indicate times when animal was in a reward zone location. These locations were not considered for further analysis. Solid and dotted black lines indicate back and forth trials respectively. Top view of animal in the maze is depicted on the right. Arrows indicate teleportation in the same position but facing opposite direction after reward consumption. Bottom: Animal's speed as a function of time. **D. E.** Box plots of the percentage of active cells (**D**; $P = 0.18$, two-tailed unpaired t-test) and place cells (**E**; $P < 10^{-4}$, two-tailed unpaired t-test) in the maze without (blue) and with (orange) objects (same color code throughout the figures). **F.** Spike raster plots (top) and color-coded firing rate map (middle) for successive trials in one direction (arrow) as a function of the position in the maze. Bottom: corresponding mean firing rate by positions. Dots indicate positions of the detected place field (see Material and Methods). **G-K.** Box plots of the place field width (**G**; $P = 0.055$, two-tailed Wilcoxon rank sum (WRS) test), the place field dispersion (**H**; $P < 10^{-4}$, two-tailed WRS test), the stability index (**I**; $P < 10^{-12}$, two-tailed WRS test), the out/in field firing rate (**J**; $P < 10^{-4}$, two-tailed WRS test) and the spatial information (**K**; $P < 10^{-9}$, two-tailed WRS test). For box plots in this and subsequent figures, box extends from the first (Q1) to the third quartile (Q3) with the band inside showing the median and the extremities of the whiskers include values greater than Q1-1.5*(Q3-Q1) and smaller than Q3 + 1.5*(Q3-Q1).

128   two-tailed WRS test; Fig. 1I). Altogether, these results demonstrate that local visual cues can

129   improve inter-trial spatial stability.

130   An increase in spatial coding resolution would also be associated with higher spatial

131   selectivity and information content. Spatial selectivity was assessed by comparing the in-

132   field versus out-of-field firing rates (i.e., signal to noise ratio) for place fields recorded in OT

133   and ØT. In the track without objects, place cells increased their firing rate inside the place

134   field (7.44 ± 0.75 Hz, n = 48 place cells) but also discharged at high rate outside the field

135   (5.23 ± 0.62 Hz; Fig. 1F and J; ratio: 0.65 ± 0.02). In comparison, place cells recorded in the

136   track with objects had comparable firing rates inside the place field (6.73 ± 0.61 Hz, n = 103

137   place cells; Z = 1.67, P = 0.1, two-tailed WRS test) but fired significantly less outside the field

138   (3.53 ± 0.49 Hz; ratio: 0.42 ± 0.02; Fig. 1F and J; Z = 3.99, $P < 10^{-4}$, two-tailed WRS test).

139   Accordingly, spatial information (in bit/spike), a measure independent of place fields'

140   detection (William E. Skaggs and Bruce L. McNaughton and Katalin M. Gothard and Etan J.

141   Markus, 1993) was very low in the track without object (0.06 ± 0.01 bit/spike, n = 48 place

142   cells) and significantly higher in the presence of objects (0.32 ± 0.03 bit/spike, n = 103 place

143   cells; Z = -6.29, $P < 10^{-9}$, two-tailed WRS test; Fig. 1K). Similar results were obtained with a

144   different method to estimate spatial information content based on the original mutual

145   information metric with a normalization to correct possible bias due to differences in basal

146   firing rates between conditions (Souza et al., 2018) (ØT: 1.66, n = 48 place cells; OT: 6.62, n =

147   103 place cells; Z = -7.36, $P < 10^{-12}$, two-tailed WRS test).

148   Altogether these results indicate that local visual cues can strongly enhance the

149   proportion of place cells among active cells but also place cell's coding accuracy in

150   agreement with an improved spatial coding resolution.

151

Virtual 3D objects improve spatial resolution locally

153   We then wondered whether 3D objects could enhance spatial resolution locally within the

154   same environment. To address this question, we focused our analysis on On-Track fields

155   recorded in the OT. We first noticed that the distribution of these fields was non-uniform on

156   the track (P = 0.001, test of non-uniformity). To quantify more precisely this effect, we

157   divided the linear track in Objects Zones (OZ) and No Objects Zones (ØZ), depending if a

158   given track zone contained an object or not, respectively (Fig. 2A, right). The density of place

159   fields was significantly higher in OZ (OZ: 8.80 ± 1.09% /10 cm, n = 12 spatial bins of 10 cm, 6

7
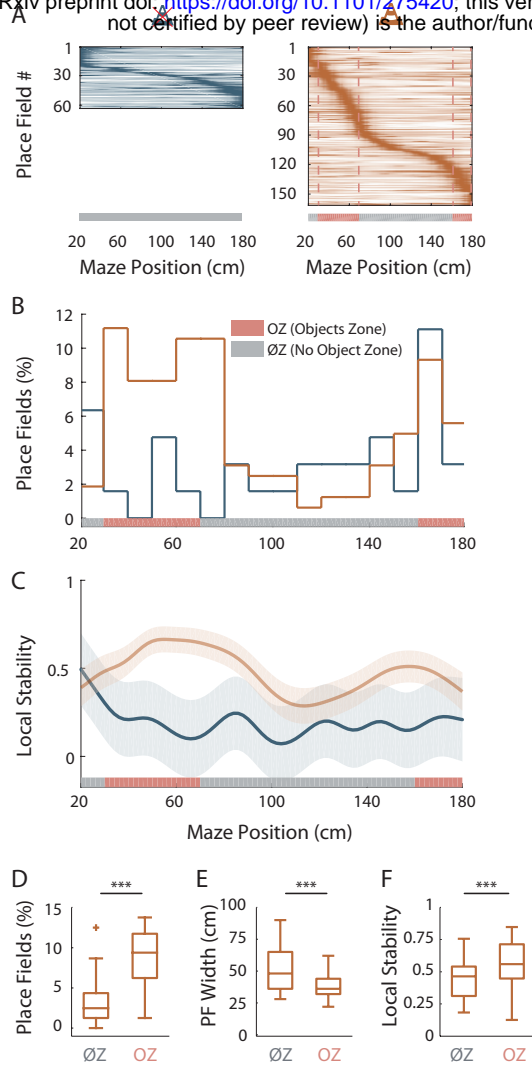
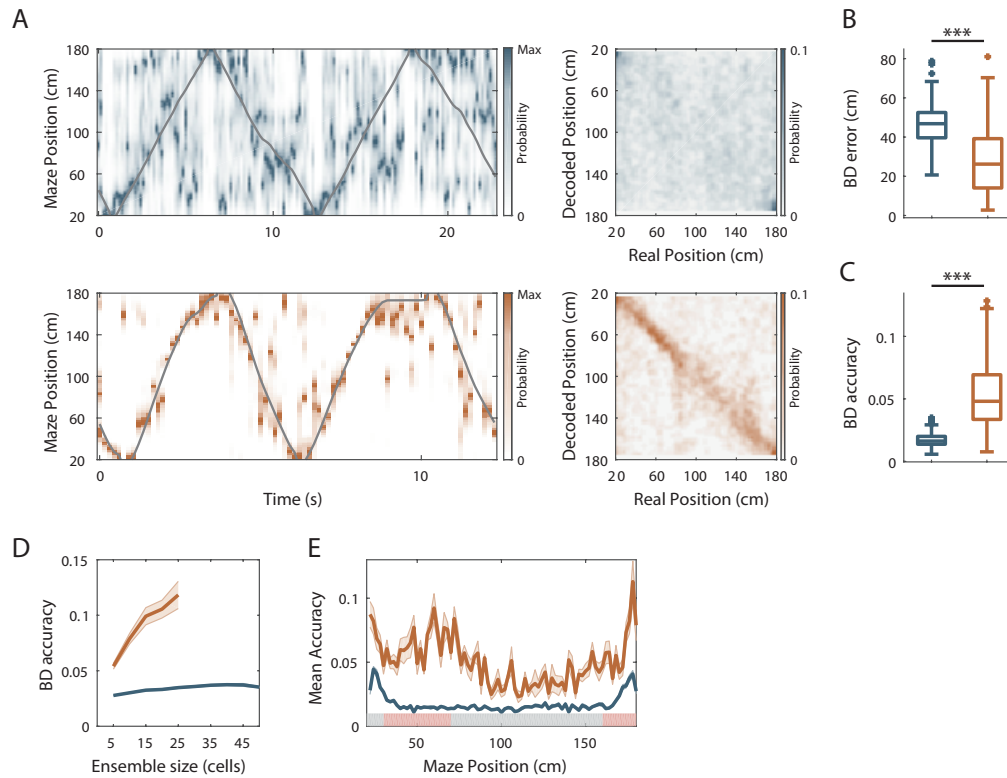## Figure 2: Virtual 3D objects improve spatial resolution locally

A. Color-coded mean firing rate maps of all place fields recorded in the maze without objects (left) or with objects (right). The color codes for the intensity of the bin's mean firing rate normalized on the maximal mean firing rate (peak rate) in the recording session. The place cells are ordered according to the position of their peak rate in the track (reward zones excluded). Bottom: The tracks were divided into Objects Zones (OZ, in red on the x-axis) around the objects and No Object Zones (ØZ, in grey on the x-axis) deprived of objects. Red dotted lines depict the boundaries of the OZ in the track with objects. **B.** Percentage of On-Track place fields at each spatial bin (10 cm) in the maze with (orange line) and without objects (blue line). **C.** Mean local stability index (solid lines) ± SEM (shaded bands) for place cells with On-Track fields at each spatial bin in the track with (orange) or without (blue) objects. **D-F.** Box plots depicting the mean percentage of place fields per spatial bin (**D**; $P < 10^{-4}$, two-tailed unpaired t-test), the place field width (**E**; $P = 0.00016$, two-tailed WRS test) and the local stability index (**F**; $P < 10^{-5}$, two-tailed WRS test) in OZ and ØZ in the maze with objects.

160   in each direction; ØZ: 3.17 ± 0.70% /10 cm, n = 20 spatial bins of 10 cm, 10 in each direction;

161   t_{30} = -4.54, $P < 10^{-4}$, two-tailed unpaired t-test; Fig. 2B and D). Furthermore, in the maze with

162   objects, place fields were significantly smaller in OZ (38.4 ± 1.46 cm, n = 50 fields) compared

163   to ØZ (51.6 ± 2.62 cm, n = 45 fields; Z = 3.71, P = 0.00016, two-tailed WRS test; Fig. 2E).

164   Accordingly, place field dispersion was also significantly reduced in OZ (7.15 ± 0.59 cm, n =

165   87 fields) compared to ØZ (10.0 ± 0.99 cm, n = 49 fields; Z = 2.53, P = 0.011, two-tailed WRS

166   test). A local stability index (see Materials and methods section) was significantly increased

167   in OZ (0.56 ± 0.02, n = 60 bins of 2 cm, 30 in each direction) compared to ØZ (0.44 ± 0.01, n =

168   100 bins of 2 cm, 50 in each direction; Z = -4.68, $P < 10^{-5}$, two-tailed WRS test; Fig. 2C and F).

169   Finally we found no significant difference in the out-of-field versus in-field firing ratio

170   between fields located in OZ or ØZ (OZ: 0.45 ± 0.03, n = 87 fields; ØZ: 0.41 ± 0.03, n = 49

171   fields; Z = -0.62, P = 0.54, two-tailed WRS test) nor changes in spatial information (OZ: 0.36 ±

172   0.04 bit/spike, n = 87 fields; ØZ: 0.28 ± 0.04 bit/spike, n = 49 fields; Z = -0.68, P = 0.50, two-

173   tailed WRS test). These results indicate that 3D objects can locally improve spatial coding

174   resolution through a local increase in place field number, a local reduction in place field size

175   and an higher local stability while their effect on spatial information content is more global.

176   We next wondered whether similar local effects on spatial coding resolution could be

177   observed in the ØT. In this track place fields were also non-uniformly distributed (P = 0; test

178   of non-uniformity) with a higher density of fields at the ends of the track (i.e. End-Track

179   fields; Fig. 2A). However, we found no significant difference between End-Track and On-

180   Track fields in terms of out-of-field versus in-field firing ratio (End-Track: 0.65 ± 0.02, n = 31

181   fields; On-Track: 0.63 ± 0.03, n = 32 fields; Z = -0.04, P = 0.97, two-tailed WRS test) and

182   stability (End-Track: 0.17 ± 0.01, n = 31 fields; On-Track: 0.15 ± 0.02, n = 32 fields; t_{61} = 0.77,

183   P = 0.45, two-tailed unpaired t-test). Spatial information was low for both types of fields but

184   paradoxically lower for End-Track fields (End-Track: 0.04 ± 0.01 bit/spike, n = 31 fields; On-

185   Track: 0.09 ± 0.02 bit/spike, n = 32 fields; Z = -2.54, P = 0.01, two-tailed WRS test). We

186   conclude that overrepresentation of the ends of the ØT is not associated with increased

187   spatial coding accuracy and is unlikely to represent increased spatial coding resolution at

188   these locations.

189

190   **Local visual cues improve hippocampal population coding accuracy**

Figure 3: Virtual 3D objects improve hippocampal population coding accuracy

A. Left: Color-coded distribution of the animal position's probability in the virtual track (the reward zones are excluded) computed using a Bayesian decoder (see Material and Methods) at each time window (500 ms) illustrated during 4 trials in the maze without (top) and with (bottom) objects. Spike trains of active cells were used to compute the animal position's probability. For visualization purpose, position probability is normalized by its maximum at each time bin. The real position is indicated with a solid grey line. Right: Confusion matrix between the real (x-axis) and the decoded position (y-axis) for all recording sessions performed on the track without objects (top) or with objects (bottom). **B.** Box plots depicting the Bayesian decoding error (BD error) in the maze with and without objects. The BD error was significantly higher in the maze deprived of objects ($P < 10^{-23}$, two-tailed WRS test). **C.** Box plots depicting the Bayesian decoding accuracy (BD accuracy) in the maze with and without objects. The BD accuracy was significantly higher in the maze with objects ($P < 10^{-41}$, two-tailed WRS test). **D.** Mean BD accuracy (solid lines) ± SEM (shaded bands) as a function of a subset of active cells in the maze with and without objects. **E.** Mean BD accuracy (solid lines) ± SEM (shaded bands) at each position in the maze with and without objects. The track was divided in two zones: Objects Zone (OZ, in red on the x axis) around the objects and No Object Zone (ØZ, in grey on the x axis) deprived of objects. Note that the decoding accuracy was specifically improved in OZ in comparison to ØZ in the maze with objects ($P < 10^{-6}$, two-tailed WRS test).

191   The results so far suggest that objects can increase the resolution of hippocampal spatial

192   representation. To verify this, we next performed position-decoding analysis (Brown et al.,

193   1998; Zhang et al., 1998) (Fig. 3A). We used the spike trains from all pyramidal cells recorded

194   (i.e., both the spatially modulated and nonspatially modulated cells) and compared decoded

195   positions with actual positions of the animal in the virtual linear tracks. Overall, the effect of

196   objects on hippocampal spatial coding was obvious because the decoding error across trials

197   was nearly two-fold larger in the track without objects compared to the track with objects

198   (ØT: 46.3 ± 0.05 cm, n = 180 trials; OT: 27.6 ± 0.12 cm, n = 129 trials; Z = 10.1, $P < 10^{-23}$, two-

199   tailed WRS test; Fig. 3A and B). Accordingly, the decoding accuracy (van der Meer et al.,

200   2010) was three fold lower in the empty track compared to the track with objects (ØT: 0.017

201   ± 2.8 X 10^{-5}, n = 180 trials; OT: 0.053 ± 2.06 x 10^{-4}, n = 129 trials; chance level 0.01; Z = -13.7,

202    $P < 10^{-41}$, two-tailed WRS test; Fig. 3A and C). In both cases, downsampling was performed to

203   equalize the number of cells used for decoding between the two conditions (20 active cells).

204   These effects were independent of the decoding method used because similar results were

205   observed using a Firing Rate Vector (FRV) method (Wilson and McNaughton, 1993;

206   Middleton and McHugh, 2016). Correlation values were lower in the empty track (ØT: 0.63 ±

207   0.008, n = 180 trials; OT: 0.74 ± 0.01, n = 129 trials; Z = -8.62, $P < 10^{-17}$, two-tailed WRS test)

208   and decoding errors were higher (ØT: 48.4 ± 0.67 cm, n = 180 trials; OT: 33.0 ± 1.81 cm, n =

209   129 trials; Z = 7.32, $P < 10^{-12}$, two-tailed WRS test). Because Bayesian decoding was

210   performed using a drop cell approach we could measure decoding accuracy for different

211   sample sizes of active cells (van der Meer et al., 2010) (Fig. 3D). Decoding accuracy was

212   positively correlated with sample size in the track with objects but not in the track without

213   objects (Fig. 3D). Importantly, in the track without objects, the decoding accuracy never

214   reached values observed for the track with objects, even when using a larger set of cells (up

215   to 45). To see if objects could locally increase spatial decoding accuracy we compared

216   decoding accuracy between OZ and ØZ. While decoding accuracy was uniformly low in the

217   track without objects (OZ: 0.019 ± 0.0014, n = 30 spatial bins of 2 cm; ØZ: 0.016 ± 9.25 x 10^{-4},

218   n = 50 spatial bins of 2 cm; Z = 1.42, P = 0.16, two-tailed WRS test; Fig. 3E), it was increased

219   in every part of the track with objects but significantly more in OZ compared to ØZ (OZ:

220   0.063 ± 0.003, n = 30 spatial bins of 2 cm; ØZ: 0.043 ± 0.002, n = 50 spatial bins of 2 cm; Z =

221   4.99, $P < 10^{-6}$, two-tailed WRS test; Fig. 3E). We concluded that local visual cues can globally

222   and locally improve spatial coding accuracy at the population level.

9
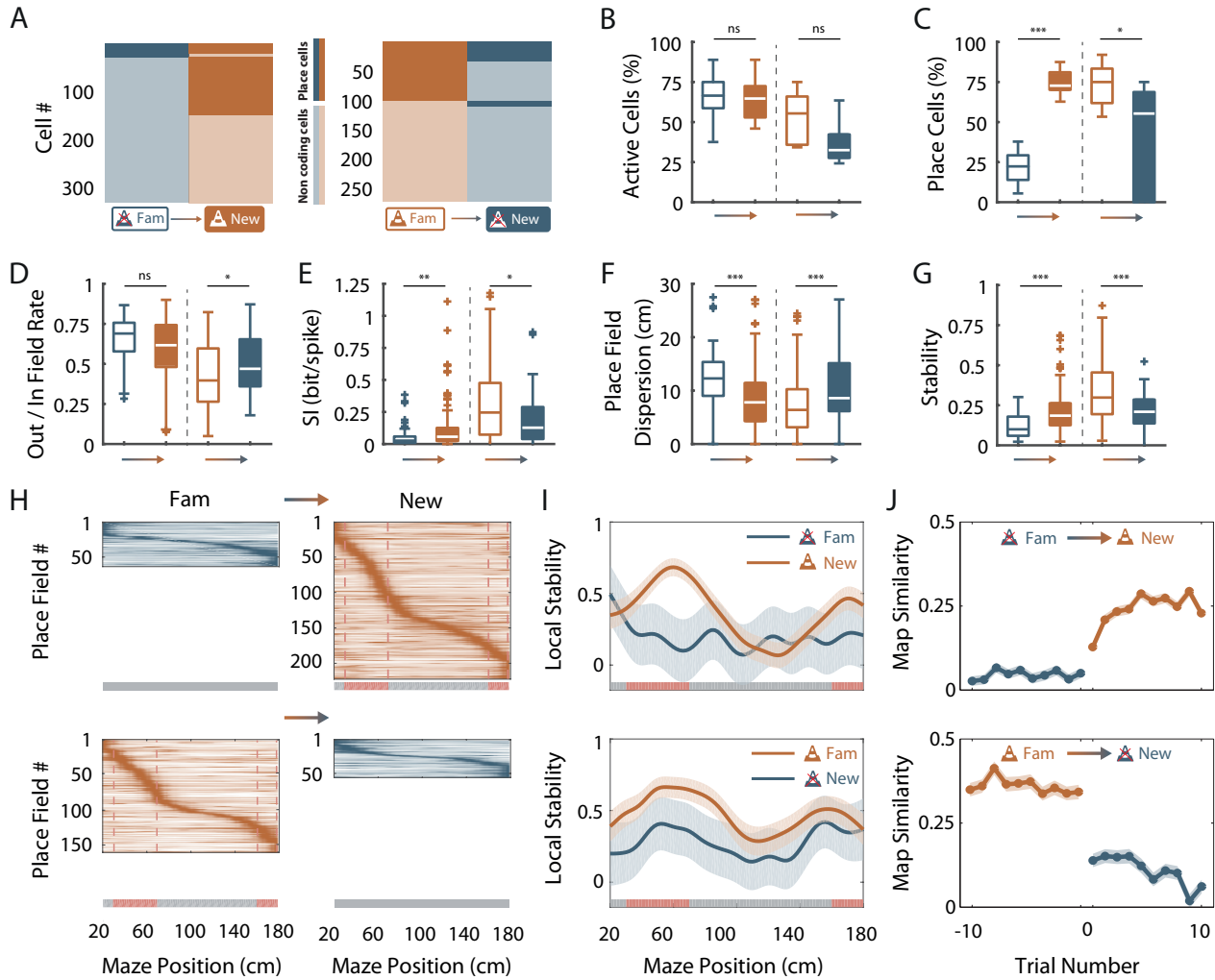
## Figure 4: Effects of online object manipulation

A. Mosaic plots representing the cells classified as place cells (darker orange and blue) or non-coding cells (i.e. silent or active non-coding, lighter orange and blue) in the familiar and the new mazes. **B-G.** Box plots comparing familiar (empty box) and new mazes (filled box) conditions. Two pairs of box plots are illustrated; Left: comparison between the familiar maze without objects (blue, ØT_{fam}) and the new maze with objects (orange, OT_{new}). Right: comparison between the familiar maze with objects (orange, OT_{fam}) and the new maze without objects (blue, ØT_{new}). A gradient color arrow shows the way of the transition. Plots show the percentage of active cells (**B;** ØT_{fam} vs OT_{new}: $P = 0.66$; OT_{fam} vs ØT_{new}: $P = 0.14$, two-tailed paired t-test), the percentage of place cells (**C;** $P < 10^{-5}$ and $P = 0.04$, respectively, two-tailed paired t-test), the Out/In field firing rate (**D;** $P = 0.06$ and $P = 0.047$, respectively, two-tailed WRS test), the spatial information (SI; **E;** $P = 0.0014$ and $P = 0.015$, respectively, two-tailed WRS test), the place field dispersion (**F;** $P < 0.0004$ and $P = 0.0008$, respectively, two-tailed WRS test) and the stability index (**G;** $P < 10^{-5}$ and $P = 0.0002$, respectively, two-tailed WRS test). **H.** Color-coded mean firing rate maps of place fields recorded in the familiar and new mazes. The color codes for the intensity of the firing rate normalized by the peak rate. The place fields are ordered according to the position of their peak rate in each track (the reward zones are excluded). The tracks were divided into Objects Zones (OZ, in red on the x-axis) around the objects and No Object Zones (ØZ, in grey on the x-axis) deprived of objects. Red dotted lines depict the boundaries of the OZ in the track with objects. **I.** Mean local stability index (solid orange or blue lines) ± SEM (blue or orange shaded areas) at each spatial bin in the familiar and new mazes (top: from ØT_{fam} to OT_{new}; bottom: from OT_{fam} to ØT_{new}). **J.** Map similarity (see Material and Methods) for 10 trials before and 10 trials after the experimental manipulation (indicated by 0) for ØT_{fam} to OT_{new} (top) and for OT_{fam} to ØT_{new} condition (bottom).

223

Effects of online virtual objects manipulation

Place cells usually appear instantaneously upon exploration of a new environment in area CA1 (Wilson and McNaughton, 1993). To see if similar dynamics could be observed for the effects of virtual objects on spatial resolution we manipulated objects online while recording the same ensemble of cells in area CA1. For mice trained in an empty track, we instantaneously added the three objects (which were thus new to the mice) after 20 back and forth trials. Conversely, for mice trained in the track with objects we instantaneously removed the three objects. Objects manipulation had no effect on the proportion of active cells (Fig. 4B) but a strong impact on the proportion of place cells (Fig. 4A and C). For mice trained in an empty track, adding objects instantaneously increased the proportion of place cells (from 21.6 ± 5.3% to 75.0 ± 4.1%; n = 5 sessions in 3 mice; t_4 = -35.8, $P < 10^{-5}$, two-tailed paired t-test; Fig. 4A and C). Thus, a large proportion of cells initially silent or active but nonspatially modulated in the familiar empty track became spatially modulated (40.3%). Most of these cells had on-track fields (81.3%; Fig. 4H). A majority of cells initially spatially modulated remained place cells (75.7%) while the others became nonspatially modulated or silent. Adding objects also increased place cells' spatial information (Z = -3.20, P = 0.0014, two-tailed WRS test; Fig. 4E) and stability (Z = -4.68, $P < 10^{-5}$, two-tailed WRS test; Fig. 4G). Local stability was significantly higher in OZ when objects were added (OZ: 0.56 ± 0.02, n = 60 bins of 2 cm, 30 in each direction; ØZ: 0.25 ± 0.02, n = 100 bins of 2 cm, 50 in each direction; Z = -8.56, $P < 10^{-16}$, two-tailed WRS test; Fig. 4I) but not before (t_{158} = 0.15, P = 0.88, two-tailed unpaired t-test). Place fields' out/in field firing ratio and dispersion were instantaneously decreased (Z = 1.86, P = 0.06 and Z = 3.55, P = 0.0004, respectively, two-tailed WRS test; Fig. 4D and F). On the other hand, removing objects decreased the proportion of place cells (from 73.1 ± 6.62% to 39.4 ± 16.4%, n = 5 sessions in 2 mice; t_4 = 2.94, P = 0.04, two-tailed paired t-test; Fig. 4A and C). The spatial information and stability were decreased by this manipulation (Z = 2.44, P = 0.015 and Z = 3.72, P = 0.0002, respectively, two-tailed WRS test; Fig. 4E and G) while place field out/in field firing ratio and dispersion were increased (Z = -1.99, P = 0.047 and Z = -3.31, P = 0.0008, respectively, two-tailed WRS test; Fig. 4D and F). However, even after object removal, local stability was still significantly higher in OZ (OZ: 0.34 ± 0.02, n = 60 bins of 2 cm, 30 in each direction; ØZ: 0.24 ± 0.02, n = 100 bins of 2 cm, 50 in each direction; t_{158} = -3.7, P = 0.0003, two-tailed unpaired

10
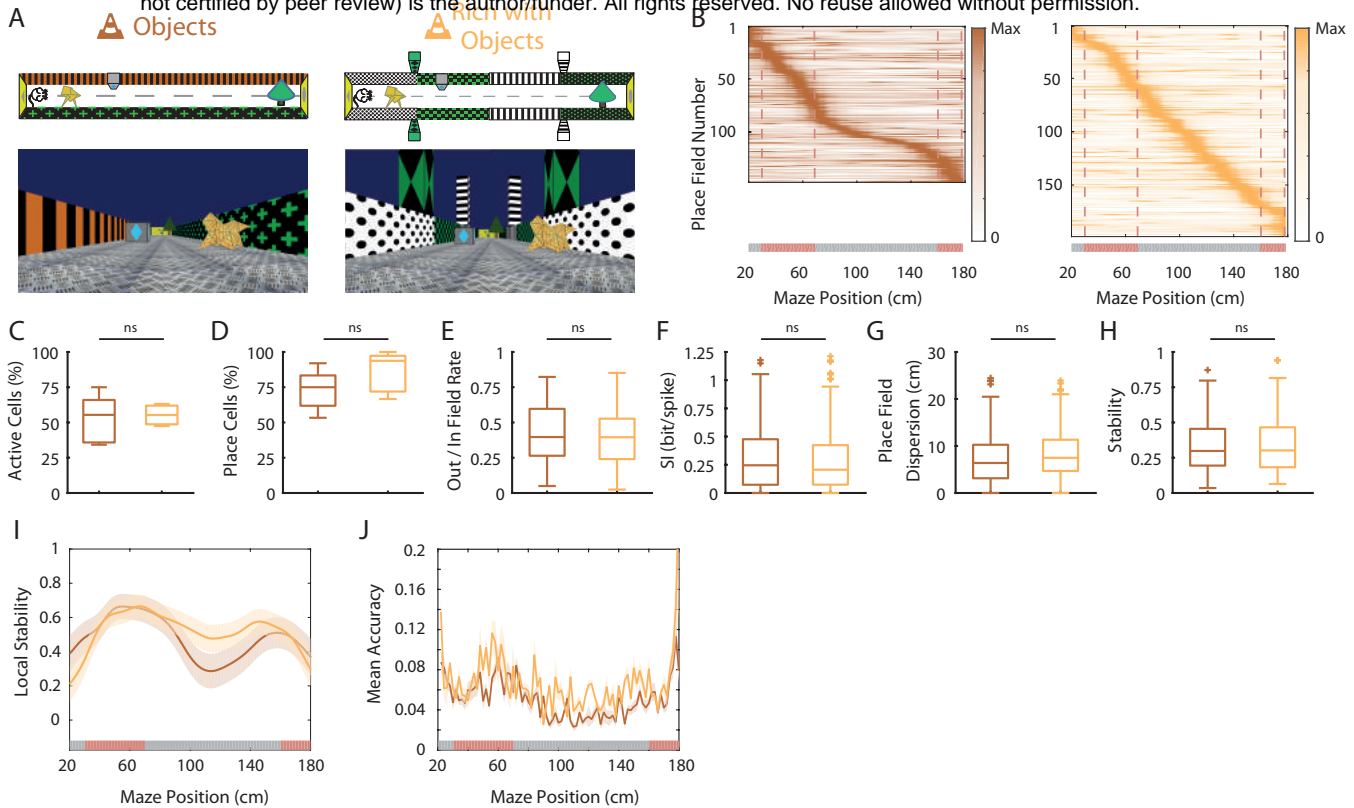
Figure 5: Effects of virtual 3D objects in a visually enriched environment

A. Schema (top) and picture (bottom) representing the original maze with objects (left) and a visually enriched maze with objects (right). **B.** Color-coded mean firing rate maps for all place fields recorded in the original maze with objects (orange, left) and on the visually rich maze with objects (yellow, right). The color codes for the intensity of the firing rate normalized by the peak rate. The place fields are ordered according to the position of their peak rate in each track (the reward zones are excluded). The tracks were divided into Objects Zones (OZ, in red on the x-axis) around the objects and No Object Zones (ØZ, in grey on the x-axis) deprived of objects. Red dotted lines depicts the boundaries of the OZ. **C-H.** Box plots representing in the original (orange) and visually rich (yellow) maze with objects the percentage of active cells (**C;** $P = 1$, two-tailed WRS test), the percentage of place cells (**D;** $P = 0.20$, two-tailed unpaired t-test), the out/in field rate (**E;** $P = 0.57$, two-tailed WRS test), the spatial information (SI; **F;** $P = 0.67$, two-tailed WRS test), the place field dispersion (**G;** $P = 0.06$, two-tailed WRS test) and the stability index (**H;** $P = 0.95$, two-tailed WRS test). **I.** Mean local stability index (solid orange or yellow lines) ± SEM (orange or yellow shaded bands) at each position's bin in the original (orange) and visually rich (yellow) mazes. **J.** Mean BD accuracy (solid lines) ± SEM (shaded bands) at each spatial bin in the original maze with objects (orange) or in the visually rich maze with objects (yellow).

255   *t*-test; Fig. 4I). We conclude that the effects of local visual cues on place cells' coding

256   observed between familiar tracks can be reproduced with instantaneous objects

257   manipulation.

258   We next investigated the dynamic of these changes by correlating the firing rate

259   maps of each back and forth trial with the corresponding average firing rate map in the

260   condition with objects (the most stable condition) for 10 trials before (t-1 to t-10) and 10

261   trials after (t+1 to t+10) the manipulation (Fig. 4J). When objects were added in the empty

262   track, map similarity was significantly higher for the second trial in the new condition (t-1 vs

263   t+1, n = 598 pyramidal cells; Z = 3.49, P = 0.09; t+1 vs t+2, n = 614 pyramidal cells; Z = 3.71, P

264   = 0.04; Kruskall-Wallis one-way test with post-hoc Bonferroni test) and then stayed higher

265   from this second trial on (t+2 vs t+3, n = 608 pyramidal cells; P = 1, Kruskall-Wallis one-way

266   test with post-hoc Bonferroni test). Conversely, when objects were removed from the

267   familiar track with objects, map similarity dropped already for the first trial in the new

268   condition (t-1 vs t+1, n = 380 pyramidal cells; $P < 10^{-8}$, Kruskall-Wallis one-way test with post-

269   hoc Bonferroni test) and stayed lower from this first trial on (t+1 vs t+2, n = 380 pyramidal

270   cells; P = 1, Kruskall-Wallis one-way test with post-hoc Bonferroni test). Thus, the

271   hippocampus can rapidly adapt its spatial coding resolution to local visual cues available in

272   the environment.

273

274   **Low proportion of landmark vector cells in OT**

275   Newly activated place cells could correspond to landmark vector (LV) cells, which have been

276   recorded in the hippocampus of freely moving rats (Deshmukh and Knierim, 2013) and head-

277   fixed mice running on a treadmill (Geiller et al., 2017). These cells tend to discharge

278   systematically near objects present in the environment or landmarks on the treadmill. To

279   test this hypothesis, we specifically looked for LV cells in our recordings. On individual

280   unidirectional trials the presence of LV cells firing near a specific object would be difficult to

281   disentangle from the firing of a place cell which happen to have a place field near that object

282   by chance. Because LV cells tend to systematically discharge near objects, these cells should

283   discharge near the same object (s) in both back and forth trials. We thus used back and forth

284   trials to address this point. We defined object zones for each individual object (IOZ, which

285   were enlarged on the side from which animals were approaching the object to take into

286   account the anticipatory nature of some LV cells (Geiller et al., 2017). Place cells were
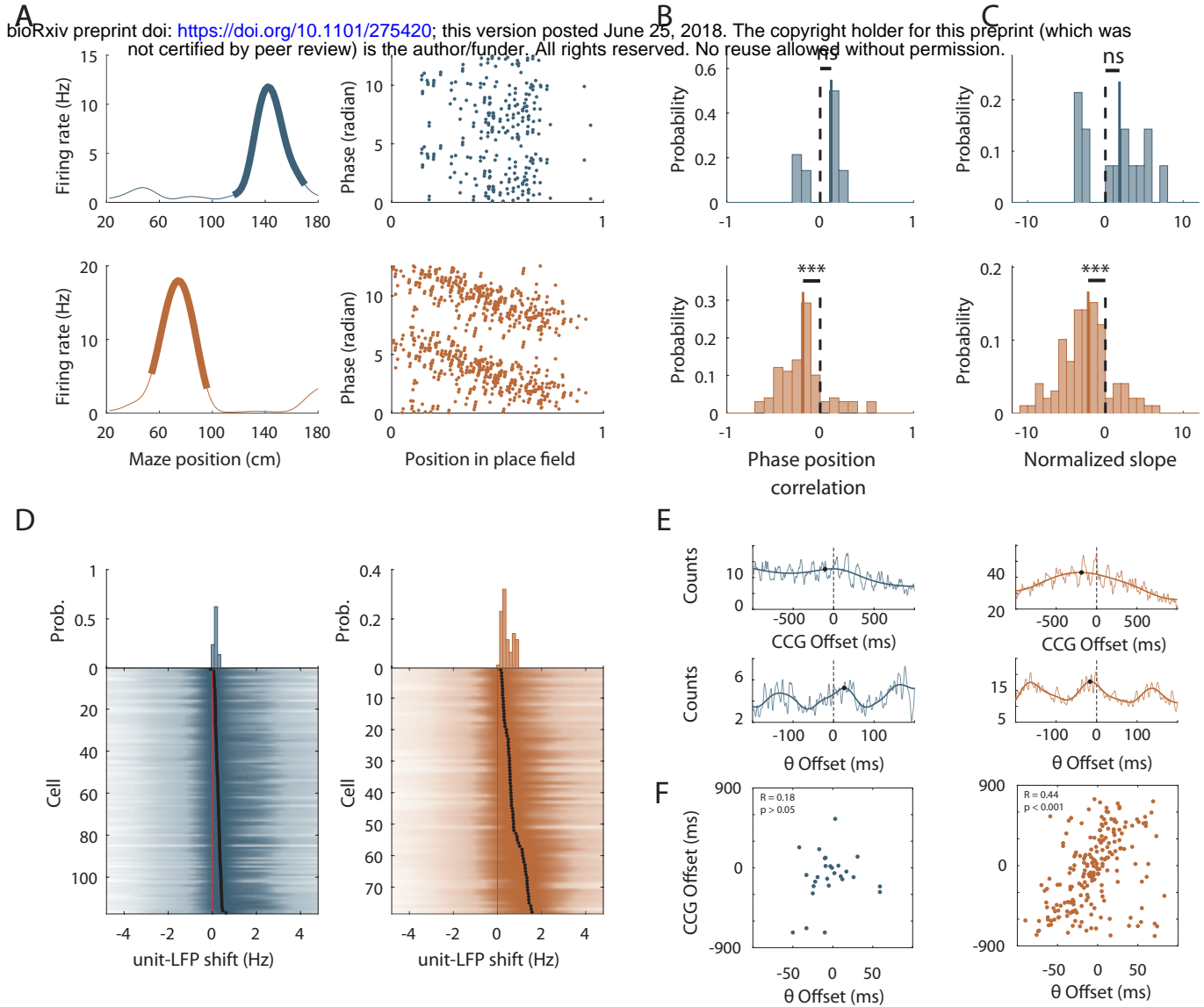
Figure 6: Importance of local visual cues for hippocampal temporal coding

A. Left: Mean firing rate maps of representative CA1 place cells with place fields highlighted by a bold line (left) recorded in the maze without objects (top, only spatially stable trials see Material and Methods section) and with objects (bottom). Right: spikes phase (radian) versus position in the corresponding place fields. **B-C.** Distribution of significant phase position correlation (**B**) and slopes (**C**) in the condition without objects (top; correlation: $P = 0.42$; slopes: $P = 0.4$, one-sample sign-test) and with objects (bottom; correlation: $P < 10^{-11}$; slopes: $P < 10^{-11}$, one-sample sign-test). The median of the distribution is indicated by a bold line and 0 by a dotted line. **D.** Color-coded cross-correlogram between the power spectra of neuronal spikes and LFP for each theta-modulated cell recorded on the maze without (bottom left, blue) and with (bottom right, orange) objects. Black dots indicate the maximum of each cross-correlation. Each cross-correlation is normalized by its maximum. Top: Distribution of the maximum cross-correlations used to quantify the frequency shift for all the cells. **E.** Examples of cross-correlograms computed for two pairs of place cells with overlapping place fields at the behavioral (top) or theta time scale (bottom , see Methods) in order to quantify Cross-Correlogram (CCG) and theta Offsets respectively in no object (blue; left) or object (orange; right) conditions. **F.** Relationship between 'CCG' and 'theta' offsets in the cross-correlograms of all the spikes in overlapping place fields of neuron pairs recorded in no object (top; blue; R = 0.18, $P = 0.377$, Pearson correlation) and object condition (bottom; orange; R = 0.44, $P < 0.001$, Pearson correlation).

287   classified as LV cells if they were bidirectional (firing in back and forth trials) and had one or

288   more place field(s) in an IOZ corresponding to the same object for back and forth trials. In

289   the track without objects no LV cells were detected. In the track with objects, LV

290   represented only 6.79% of all place cells. This corresponds to the proportion of LV cells

291   recorded in area CA1 in the presence of real objects (Deshmukh and Knierim, 2013). Thus,

292   the vast majority of newly activated place cells in the presence of objects does not behave

293   like LV cells.

294

295   **Effects of virtual objects in a visually enriched environment**

296   We next wondered whether the hippocampal mapping resolution was maximal in the

297   presence of objects or whether it could be further increased by visually enriching the

298   environment. We thus analyzed hippocampal place cells' coding in another environment

299   containing the original 3D objects but enriched in visual cues such as different wall patterns

300   in different positions along the track and high 3D columns outside the track (EOT, n = 3 mice;

301   Fig. 5A). The percentage of active cells was not increased by visually enriching the

302   environment (OT, n = 5 sessions in 2 mice; EOT, n = 5 sessions in 3 mice; Z = -0.1, P = 1, two-

303   tailed WRS test; Fig. 5C) nor was the percentage of place cells (OT, n = 5 sessions in 2 mice;

304   EOT, n = 5 sessions in 3 mice; t_8 = -1.38, P = 0.20, two-tailed unpaired t-test; Fig. 5B-D).

305   However, place fields were uniformly distributed along the track in the visually rich

306   environment (n = 16 spatial bins of 10 cm; P = 0.23, test for non-uniformity), thus not

307   clustered around objects as in the visually poor environment (Fig. 5B). This suggests that

308   local visual cues are important to set place fields' position (Renaudineau et al., 2007).

309   However, all other attributes of place fields were not significantly different between the two

310   environments (OT, n = 103 place cells; EOT, n = 132 place cells; out/in field firing ratio: Z =

311   0.57, P = 0.57; Spatial info: Z = 0.42, P = 0.67; Dispersion: Z = -1.88, P = 0.06; Stability: Z = -

312   0.06, P = 0.95; two-tailed WRS test for all; Fig. 5E-H). When looking at local stability of firing

313   rates, we still observed a significant effect of objects in the visually enriched environment in

314   OZ versus ØZ (OZ, n = 60 spatial bins of 2 cm; ØZ: n = 100 spatial bins of 2 cm; Z = -2.46, P =

315   0.014, two-tailed WRS test; Fig. 5I). Interestingly, positions near objects were also decoded

316   with a better accuracy using a Bayesian decoder than positions further away in the visually

317   enriched environment (OZ: 0.08 ± 0.007, n = 30 spatial bins of 2 cm; ØZ: 0.059 ± 0.002, n =

318   50 spatial bins of 2 cm; Z = 3.08, P = 0.002, two-tailed WRS test; Fig. 5J). Altogether these

319   results suggest that in the presence of local visual cues, hippocampal spatial coding is not

320   further improved by visually enriching the environment. However, place fields locations are

321   influenced by additional visual cues along the track. Interestingly, despite a homogeneous

322   distribution of place field locations, 3D objects could still locally influence hippocampal

323   population decoding accuracy.

324

325   **Hippocampal phase precession is strongly reduced in the absence of virtual**

326   **3D objects**

327   The results so far suggest that local 3D objects can increase spatial coding resolution when

328   considering the spatial firing rate code. Place cells however do not only increase their firing

329   rate inside the place field but also tend to fire at progressively earlier phases of the theta

330   oscillation as an animal moves through the place field (O'Keefe and Recce, 1993). This

331   phenomenon, called theta phase precession, is thought to further increase spatial coding

332   resolution because different locations within the place field that are difficult to distinguish

333   based on firing rate alone can be accurately separated when phase is taken into account. In

334   the temporal domain, increased spatial resolution would thus correspond to increased slope

335   of the phase versus position relationship for identical field sizes.

336   We first looked for differences in the theta oscillation recorded in the Local Field

337   Potential (LFP) between the two conditions. The mean frequency of the field theta

338   oscillation was not significantly different when mice were running in the track with or

339   without objects (ØT: 6.79 ± 0.12 Hz, n = 9 sessions in 3 mice; OT: 6.77 ± 0.10 Hz, n = 5

340   sessions in 2 mice; Z = 1.14, P = 0.30, two-tailed WRS test) but was lower than that reported

341   for mice navigating in real linear tracks (Middleton and McHugh, 2016). The power of theta

342   oscillation (theta index see Materials and methods section) was also not significantly

343   different (ØT: 3.31 ± 0.23, n = 9 sessions in 3 mice; OT: 3.55 ± 0.22, n = 5 sessions in 2 mice;

344   t_{12} = -0.69, P = 0.50, two-tailed unpaired t-test). Theta frequency was not modulated by

345   running speed of the animal in ØT (r = 0.02 ± 0.02, n = 9 sessions in 3 mice; Figure 6- figure

346   supplement 1A, C) as previously observed in virtual linear tracks when only distal cues are

347   present (Ravassard et al., 2013). Theta frequency-speed modulation was however significant

348   in OT (r = 0.14 ± 0.03, n = 5 sessions in 2 mice; t_{12} = -2.99, P = 0.01, two-tailed unpaired t-

349   test; Figure 6- figure supplement 1A, C). In contrast, theta amplitude was similarly

13

350   modulated by running speed in both conditions (ØT: r = 0.06 ± 0.03, n = 9 sessions in 3 mice;

351   OT: r = 0.1 ± 0.04, n = 5 sessions in 2 mice; t_{12} = 0.12, P = 0.9, two-tailed unpaired t-test;

352   Figure 6- figure supplement 1B, D). The proportion of active putative pyramidal cells with

353   significant theta modulation was not different between conditions (ØT: 92.8%, n = 361 active

354   cells; OT: 90.3%, n = 155 active cells; χ^2 = 0.91, df = 1, P = 0.34, Chi-Square test). The coupling

355   of spikes to theta oscillation was also not significantly different between conditions in terms

356   of preferred phase (ØT: 200.26° ± 2.6, n = 361 active cells; OT: 198.66° ± 4.12, n = 155 active

357   cells; F = 0.08, P = 0.77, circular ANOVA; Figure 6-figure supplement 2A, B) and strength

358   (mean resultant vector length ØT: 0.18 ± 0.006, n = 361 active cells; OT: 0.19 ± 0.009, n = 155

359   active cells; Z = -1.63, P = 0.1, two-tailed WRS test; Figure 6-figure supplement 2A, C).

360   We then analyzed place cells' theta phase precession. To compensate for decreased

361   spatial stability in the ØT condition we took into account only trials with good correlation

362   with the average place fields (Spatially Stable Trials or SST) for place cells recorded in the

363   empty track (Schlesiger et al., 2015), but included all trials for place cells recorded in the

364   track with objects. The stability index of SST fields in ØT was not significantly different from

365   the stability index of all fields in OT (ØT, n = 52 SST fields; OT, n = 151 fields; Z = 0.18, P =

366   0.86, two-tailed WRS test). The percentage of fields with significant (P < 0.05) and negative

367   correlation between phase and position (i.e., precessing fields) was high in the track with

368   objects (41.9%), comparable to that observed in real linear tracks in mice but low in the

369   empty track (8%; χ^2 = 15.21, df = 1, P < 10^{-4} compared to OT, Chi-Square test). Accordingly, the

370   correlation between phase and position was significantly different from zero for place cells

371   recorded in the track with objects (r = -0.18 ± 0.018, n = 99 fields; P < 10^{-11}, one sample sign-

372   test; Fig. 6A and B) but not for those recorded in the track without objects (r = 0.03 ± 0.026,

373   n = 14 fields; P = 0.42, one sample sign-test; Fig. 6A and B). Moreover, phase precession

374   slopes (calculated on normalized place field sizes) were negative and significantly different

375   from 0 for cells recorded in the track with objects (-2.43 ± 0.23 rad/U, n = 99 fields; P < 10^{-11},

376   one sample sign-test; Fig. 6C) but not in the track without objects (1.18± 0.50 rad/U, n = 14

377   fields; P = 0.4, one sample sign-test; Fig. 6C).

378   In the track without objects, the decrease in phase-position correlation could result

379   from the higher inter-trial spatial dispersion, which could lead to spikes at different theta

380   phases for identical positions. To assess this possibility, we performed phase-precession

381   analysis on single-trial-detected fields and averaged the slopes of individual passes (Schmidt

14

382   et al., 2009). The correlation was still negative and significantly different from 0 in OT (r = -

383   0.19 ± 0.29, n = 92 single-trial fields; t_{91} = -4.53, $P < 10^{-4}$, one sample t-test) but not in ØT (r =

384   -0.004 ± 0.03, n = 35 single-trial fields; t_{34} = -0.92, P = 0.92, one sample t-test). Similarly, the

385   slope of the regression line was negative and significantly different from 0 in OT (-2.27 ± 0.56

386   rad/U, n = 92 single-trial fields; P = 0.004, sign-test) but not in ØT (0.79 ± 0.56, n = 35 single-

387   trial fields; P = 0.73, sign-test).

388   Because a low percentage of active cells were place cells in the track without objects,

389   we ran an additional analysis that is independent of place field detection. It exploits the fact

390   that phase precessing cells emit theta paced spikes at a frequency slightly faster than the

391   concurrent LFP theta oscillation (O'Keefe and Recce, 1993). We performed cross-correlation

392   between the power spectra of neuronal spikes and LFP for all active cells with significant

393   theta modulation of spiking activity (ØT: 117/342 cells = 34.2%; OT: 78/142 cells = 54.9%; χ^2

394   = 17.9, df = 1, $P < 10^{-4}$, Chi-square test) and compared the frequency shift (>0) between

395   spiking and LFP theta oscillations between the two conditions (Geisler et al., 2007) (Fig. 6D).

396   The shift was significantly higher in the OT (0.72 ± 0.05 Hz, n = 78 active cells. Fig. 6D) versus

397   ØT (0.26 ± 0.01 Hz, n = 117 active cells; Z = -8.73, $P < 10^{-17}$, two-tailed WRS test; Fig. 6D).

398   Altogether, these results suggest that local visual cues are important for proper theta phase

399   precession in the hippocampus.

400   To further investigate the effect of local visual cues on temporal coding we next

401   focused on theta-timescale spike coordination. Previous studies have reported, for place

402   cells with overlapping place fields, a positive correlation between the physical distance

403   separating their place fields' centers and the time (or phase) lag of their spikes within

404   individual theta cycles (Skaggs et al., 1996; Dragoi and Buzsáki, 2006). Our analysis revealed

405   a strong correlation between theta phase and physical distance in the presence of virtual 3D

406   objects (OT: R = 0.44, n = 214 pairs in 2 mice; $P < 10^{-10}$, Pearson correlation; Fig. 6E, F) but not

407   otherwise (ØT: R = 0.18, n = 27 pairs in 3 mice; P = 0.38, Pearson correlation; Fig. 6E, F).

408   These results show that local visual cues are important for temporal coding in the

409   hippocampus beyond theta phase precession.

410

411

412

Discussion

Our study aimed at determining whether local sensory cues could influence hippocampal spatial coding resolution. We found that local sensory cues could increase spatial coding resolution through an increase in the proportion of spatially selective place cells among active cells but also enhanced place fields' spatial selectivity and stability. These effects were local within the same environment and dynamic upon cue manipulations. Local sensory cues also proved to be important for temporal place cell coding such as theta phase precession and theta timescale spike coordination.

Spatial resolution can be improved by pooling information across neurons (Wilson and McNaughton, 1993). We found that local visual cues could dramatically increase the number of place cells among active cells (by a 3-fold factor). The mechanisms of place cell activation are not fully understood. Using sensory-based models of place cells activation (Hartley et al., 2000; Strösslin et al., 2005; Barry et al., 2006; Sheynikhovich et al., 2009) one can predict that an increase in the quantity/quality of sensory cues in an environment will enhance the number of place cells coding that environment (Geva-Sagiv et al., 2015). However, previous studies using local enrichment with multimodal sensory cues or real objects reported only weak or no effects on dorsal hippocampal cell activity. One study recording in rats navigating between cue rich and cue poor parts of the same track reported no effect on the proportion of place cells or on the density of place fields (Battaglia, 2004). Furthermore, population vector analysis did not reveal a better disambiguation of nearby locations in the cue rich part of the track compared to the cue poor suggesting similar spatial coding resolution (Battaglia, 2004). Others studies found no overall increase of place cells proportion in 2D environment containing real objects nor a specific bias for place cells to fire near the objects (Renaudineau et al., 2007; Deshmukh and Knierim, 2013). One possibility to explain the lack of recruitment of additional cells in these studies could be a high recruitment rate of the dorsal hippocampus even in the "cue poor" condition due to the presence of uncontrolled local cues (Ravassard et al., 2013).

We found that place field density was specifically increased near objects. However, studies so far have revealed an homogeneous allocation of place fields in space (Muller et al., 1987; Rich et al., 2014) in a given environment. Locally activated place cells could correspond to landmark vector (LV) cells, which tend to discharge unspecifically near several

16

444   objects or landmarks in a given environment. However, the proportion of these cells is

445   generally low in the dorsal hippocampus (between 6-8 %) which is in line with the fact that

446   places near real objects are not overrepresented at the population level. We note however

447   that this proportion may vary depending on the recording location along both the proximo-

448   distal axis and radial axis. For example, the distal part of CA1, closer to the subiculum, is

449   more heavily innervated by the lateral entorhinal cortex where LV cells were first discovered

450   (Deshmukh and Knierim, 2011) and which is believed to feed information about the "what"

451   visual stream to the hippocampus (Knierim et al., 2013). Extracellular recordings specifically

452   targeting this area in the intermediate hippocampus reported an increased proportion of

453   place cells in the presence of objects (Burke et al., 2011). Whether virtual objects are

454   perceived by mice as real objects is unclear. They notably lack the multisensory component

455   inherent to real objects (Connor and Knierim, 2017). Nevertheless, they triggered a large

456   (50%) increase in place cell's proportion which is not compatible with the modest proportion

457   of LV cells reported in our and previous studies.

458   Instead, our results are more compatible with the hippocampal mapping system

459   using local visual cues to improve its spatial coding resolution. Consistent with this

460   hypothesis, spatial coding was not only quantitatively but also qualitatively increased with a

461   higher spatial selectivity, spatial information content and stability of place fields. Previous

462   studies have reported overrepresentations near rewarded location (O'Keefe and Conway,

463   1978; Hollup et al., 2001; Dupret et al., 2010; Danielson et al., 2016; Sato et al., 2018) or

464   specific sensory cues (Wiener et al., 1989; Hetherington and Shapiro, 1997; Sato et al.,

465   2018). Importantly we could also observe overrepresentations of the ends of the maze in ∅T,

466   where rewards are delivered and which are associated with prominent visual cues.

467   Nevertheless, End-track fields had a low spatial information content and stability when

468   compared to fields recorded in OT (but similar to On-track fields recorded in the same

469   maze). This argues against increased spatial coding resolution at these locations and further

470   suggests a possible dissociation between overrepresentation and increased spatial coding

471   resolution. Finally, improved coding resolution near objects could be instantaneously tuned

472   upon object manipulation while overrepresentations of specific sensory stimuli or rewarded

473   locations usually takes several days to develop (Le Merre et al., 2018; Sato et al., 2018).

474   A previous study specifically compared place cell coding in real and virtual reality

475   environments with distal visual cues only in rats (Ravassard et al., 2013). They reported a

17

476 lower number of spatially modulated cells and lower spatial selectivity in the virtual

477 environment and concluded that distal visual cues alone are not sufficient to fully engage

478 the hippocampal mapping system. Our results complement this study by showing that local

479 visual cues, on the other hand, can increase the proportion of spatially modulated cells (i.e.

480 place cells) among active cells and spatial selectivity. Several factors could explain the

481 specific effect of local visual cues on spatial coding observed in the present study. First,

482 objects could constitute a stable reference point in space to refine estimation of the current

483 subject's position possibly through anchoring of the path integrator system (McNaughton et

484 al., 2006; Poucet et al., 2015). Close to the objects, this effect could be further reinforced

485 through motion parallax effect. Second, objects as local visual cues have a higher sensory

486 resolution compared to distal visual cues. This can lead to increased spatial coding resolution

487 according to sensory based models of place cell activation (Hartley et al., 2000; Strösslin et

488 al., 2005; Barry et al., 2006). Accordingly, animals tend to increase their sensory sampling

489 rate in order to get a better sensory resolution near important locations (Geva-Sagiv et al.,

490 2015). Third, objects as salient cues in the environment could modify the attentional state of

491 the animal and favor spatial awareness. Such rise in attention has been shown to increase

492 spatial selectivity in mice (Kentros et al., 2004). However, we note that animals were not

493 required to pay close attention to objects locations to perform the task, as task performance

494 was not different between the ØT and OT conditions. Alternatively, objects could represent

495 a source of additional noise in the system thus requiring a higher number of spatially

496 modulated cells and increased spatial selectivity for efficient position coding. However,

497 position decoding was very poor in the maze without objects, which argues against this

498 possibility.

499   The effects of local cues on spatial coding accuracy were even more pronounced in

500 the temporal domain. Indeed, in the absence of local cues theta phase precession was

501 strongly reduced as observed in rat running in place on a wheel (Hirase et al., 1999) despite

502 the presence of place fields. When local cues were included, however, hippocampal place

503 cells precessed at a rate comparable to that observed in real environments (Middleton and

504 McHugh, 2016). To ascertain that this effect did not result from changes in place fields'

505 quality, additional analysis, independent of place fields' detection, were performed (Geisler

506 et al., 2007). These analyses also showed that in the presence of local cues individual cells'

507 firing tended to oscillate faster than theta oscillation recorded in the LFP, a sign of theta

18

508   phase precession while this was much less the case in the absence of local cues. Importantly
509   the frequency and power of the theta oscillation recorded in the LFP and the coupling of
510   putative pyramidal cells' firing to this oscillation were also not significantly different
511   between conditions and cannot explain observed differences. The only difference was an
512   attenuation of theta frequency speed modulation in the absence of local cues while theta
513   amplitude vs speed modulation was equivalent in both conditions. A similar absence of theta
514   frequency vs speed modulation (with intact theta amplitude vs speed modulation) was
515   observed in rats navigating virtual reality environments in the absence of local visual cues
516   (Ravassard et al., 2013). However, in this study, theta phase precession was unaffected.
517   Thus, the link between an absence of theta frequency vs speed modulation and reduced
518   theta phase precession is not straightforward. Future studies are needed to decipher the
519   mechanisms of the effect of local cues on theta phase precession. Theta phase precession is
520   thought to be involved in the generation of theta sequences, where the time lags between
521   spikes of place cells with overlapping place fields are proportional to the distance separating
522   those fields. This so-called theta sequence compression is thought to be important for
523   spatial memory. Here we found that theta timescale coordination could be observed in the
524   presence of 3D objects only. This suggests that local sensory cues are important for temporal
525   coding beyond theta phase precession.

526   Altogether, our results show enriching an environment with local visual cues allows
527   coding at higher spatial resolution with a high number of spatially modulated cells, smaller
528   firing fields, increased spatial selectivity and stability and good theta phase precession/theta
529   timescale spike coordination. The use of virtual reality raises a growing interest in the field of
530   neuroscience to study spatial cognition in rodents but also in non-human and human
531   primates (Epstein et al., 2017). Our results suggest that enriching these environments with
532   local visual cues could help comparing spatial coding in real and virtual environments.

533   We observed that local visual cues induce a rescaling of spatial coding which is both
534   global and local. What would be the benefit of this rescaling? In the wild, rodents can travel
535   kilometers away from their home to food locations through empty fields (Taylor, 1978).
536   Mapping all parts of explored environment at high resolution would require a very large
537   number of neurons and computational power (Geva-Sagiv et al., 2015). Accordingly, place
538   fields tend to be larger in bigger environments (Fenton et al., 2008) and the statistics of new
539   place cells recruitment as an environment becomes bigger are non-uniform (Rich et al.,

19

540   2014). Thus there might be a computational benefit to be able to map at high resolution

541   important places like home base or food locations and to map at lower resolution long

542   transition routes between those locations (Geva-Sagiv et al., 2015). Such resolution could

543   depend on the number of local sensory information as presented here. Future work should

544   decipher whether increased spatial coding resolution is associated with better navigational

545   accuracy and spatial memory.

Materials and methods

Animals

All experiments were approved by the Institut National de la Santé et de la Recherche Médicale (INSERM) animal care and use committee and authorized by the Ministère de l'Education Nationale de l'Enseignement Supérieur et de la Recherche (agreement number 02048.02), in accordance with the European community council directives (2010/63/UE). Data were acquired from 8 male mice C57BL/6J (Janvier/Charles River) between 8 and 12 weeks during the recording phase (weight: 21 – 23.6 g). The mice were housed 2 or 3 per cages before the first surgery and then individually with 12 inverted light/dark cycles. Trainings and recordings occurred during the dark phase.

Surgical procedure to prepare head fixation

A first surgery was performed to implant a fixation bar later used for head-fixation. Animals were anesthetized with isoflurane (3%) before intraperitoneal injection of ketamine (100 mg/Kg) mixed with xylazine (10 mg/Kg) supplemented with a subcutaneous injection of buprenorphine (0.06 mg/Kg). Two jeweller's screws were inserted into the skull above the cerebellum to serve as reference and ground. A dental cement hat was then constructed leaving the skull above the hippocampi free to perform the craniotomies later on. The free skull was covered with a layer of agarose 2% (wt/vol) and sealed with silicon elastomer (Kwik-Cast, World Precision Instruments). A small titanium bar (0.65 g; 12 x 6 mm) was inserted in the hat above the cerebellum to serve as a fixation point for a larger head plate used for head fixation only during trainings and recordings.

Virtual reality set up

A commercially available virtual reality system (Phenosys Jetball-TFT) was combined with a custom designed 3D printed concave plastic wheel (center diameter: 12.5 cm; side diameter: 7.5 cm; width: 14 cm, covered with silicon-based white coating) to allow 1D movement with a 1/1 coupling between movement of the mouse on the wheel and movement of its avatar in the virtual reality environment. This solution was preferred to the original spherical treadmill running in a X-only mode (which takes into account only rotations of the ball in the X axis to actualize the position of the avatar in the virtual reality environment) which also

21

578   allows 1D movement but with a more variable coupling between movement of the mouse

579   on the treadmill and its avatar in the virtual reality environment. The wheel was surrounded

580   by six 19-inches TFT monitors, which altogether covered a 270 degrees angle. Monitors were

581   elevated so that the mice's eyes level corresponded to the lower third of the screen height

582   to account for the fact that rodents field of view is biased upward. The head fixation system

583   (Luigs and Neumann) was located behind the animal to not interfere with the display of the

584   virtual reality environment. The virtual reality environment was a virtual 200 cm long and 32

585   cm wide linear maze with different patterns on the side and end walls and virtual 3D objects

586   (see virtual reality environments section). Movement of the wheel actualized the mouse's

587   avatar position. The mouse could only perform forward or backward movements but could

588   not turn back in the middle of the track (see training section).

589

590   **Virtual reality environments**

591   *No Object Track (ØT)*

592   Each side wall had a unique pattern (black and orange stripes on one wall; green crosses on

593   black background on the other wall). End-walls had grey triangular or round shapes on a

594   yellow background (Fig. 1A).

595   *Object Track (OT)*

596   This maze was identical to the ØT maze concerning wall patterns and dimensions but 3

597   virtual objects were included on the sides between the animal trajectory and the walls (Fig.

598   1A). The objects were a yellow origami crane (dimensions: 9 x 9 x 7 cm; position: 37 cm from

599   end wall), a blue and grey cube (dimensions: 5 x 5 x 5 cm; position: 64 cm from end wall) and

600   a tree (15 x 15 x 22 cm; position: 175 cm from end-wall). The animal could neither orient

601   toward the objects nor get any sensory feedback from them by any other mean but vision.

602   *Enriched Objects Track (EOT)*

603   This maze had the same dimensions as previous mazes and included the same virtual reality

604   objects (identical dimensions and locations than in the previous maze) but the side walls had

605   distinct symmetrical patterns in different locations along the maze (50 cm long; black dots

606   on white background, black and green squares, black and white stripes and green crosses on

607   black background). Outside the maze walls, two large 3D columns were positioned on each

608   side (dimensions 8 x 8 x 47 cm; positions 58 and 143 cm from end wall) to provide additional

609   visual cues.

22

610

Training

Mice were first habituated to the experimentalist through daily handling sessions of 20 min or more that continued throughout the experiment. After a 3 days post-surgery recovery period, mice were water-deprived (1 ml/day, including the quantity of water taken during the training). After 2-3 days of water deprivation, they were progressively trained to run in the virtual reality set up. First, mice were familiarized with running head-fixed on the wheel for water rewards in a black track (screens always black). During these sessions, animals received as a reward sweetened water (5% sucrose) for each 50 centimeters run on the wheel. When animals were comfortable with the setup, they were trained to run in one of three linear virtual tracks (familiar track) assigned randomly. When animals reached the end of the track, a liquid reward delivery tube extended in front of the animal and animal had to lick to get the reward (a 4 µL drop of water of 5% sucrose). Animals were then teleported in the same position but facing the opposite direction of the maze and had to run up to the end of the maze in the opposite direction to get another reward. Animals were initially trained during 15 minutes sessions. Session time was progressively increased to reach 60 minutes. *Ad libidum* water access was restored if the weight of the animal decreased beneath 80% of the pre-surgery weight at any stage during training.

628

Recording procedure

When animals reached a stable behavioral performance (at least 1 reward/minute during 60 minutes), we performed acute recordings using silicon probes (4/8 shanks; A-32/A-64 Buzsaki Probe, Neuronexus). On the day before recording, animals were anesthetized (induction: isoflurane 3%; maintenance: Xylazine/Ketamine 10/100 mg/Kg supplemented with Buprenorphine 0.1 mg/Kg) and a craniotomy was drilled above one hippocampus (centered on a location -2 mm posterior and ± 2.1 mm lateral from bregma). The craniotomy was covered with agarose (2% in physiological saline) then sealed with silicon elastomer (Kwik-Cast, World Precision Instruments). On the day of the recording the backside of the probe's shanks was covered with a thin layer of a cell labeling red-fluorescent dye (DiI, Life technologies) so that its location (tips of the shanks) could be assessed post-hoc histologically. The silicon probe was then lowered into the brain while the animal was

641 allowed to walk freely on the wheel with the screens displaying a black background. The

642 good positioning of the probe with recording sites in the CA1 pyramidal cell layer was

643 verified by the presence of multiple units showing complex spike bursts on several

644 recordings sites and the recording of sharp-wave ripples during quiet behavior. After

645 positioning of the silicon probe the virtual reality environment was displayed on the screen.

646 All mice (n = 8) experienced first the familiar environment (either ØT, OT or EOT) for around

647 20 back and forth trials. For mice trained in ØT or OT (n = 3 and 2, respectively), this first

648 exploration was followed, after 3 minutes of free running with the screens displaying a black

649 background, by exploration of a new environment, identical to the previous one except for

650 the presence of the three 3D objects (objects were added for mice trained in ØT and

651 removed for mice trained in OT) for another 20 consecutive back and forth trials. For some

652 of these mice (n = 2 for EOT, n = 1 for OT and n = 2 for ØT) sessions in the familiar track and

653 novel track were divided into two sub-sessions interleaved by 3 min of free running with the

654 screens black. The two sub-sessions in the familiar environment and the new environment

655 were pulled together for analysis. Note that animals stayed head-fixed on the wheel

656 surrounded by screens during the entire recording session.

657

658 **Data Acquisition and Pre-Processing**

659 The position of the animal in the virtual maze was digitalized by the virtual reality controlling

660 computer (Phenosys) and then sent to a digital-analog card (0-4.5V, National Instrument

661 Board NI USB-6008) connected to the external board (I/O Board, Open Ephys) of a 256

662 channels acquisition board (Open Ephys). Neurophysiological signals were acquired

663 continuously on a 256-channels recording system (Open Ephys, Intan Technologies,

664 RHD2132 amplifier board with RHD2000 USB interface board) at 25,000 Hz. Spike sorting

665 was performed semi-automatically using KlustaKwik (Rossant et al., 2016;

666 https://github.com/klusta-team/klustakwik). Clusters were then manually refined using

667 cluster quality assessment, auto- and cross-correlograms, clusters waveforms and similarity

668 matrix (Klustaviewa(Rossant et al., 2016).

669

670 **Data Analysis**

671   All subsequent analyses were conducted using custom-developed softwares written in

672   MATLAB (MathWorks).

673   **Reward & Object Zones Definition**

674   The reward zones, located between the maze extremities and 10% of the track length (0-20

675   cm and 180-200 cm), were not considered in the analysis. The object zone was composed of

676   two zones, one from 30 to 70 cm including both the origami crane and the cube and the

677   other from 160 to 180 cm including the tree.

678   **Firing Rate Map**

679   The maze was divided into 100 spatial bins measuring 2 cm. For each trial, the number of

680   spikes and the occupancy time of the animal in each spatial bin were calculated to obtain the

681   spikes number vector and the occupancy time vector, respectively. These vectors were

682   smoothed using a Gaussian filter with a half-width set to 10 spatial bins. Spikes occurring

683   during epochs when velocity was lower than 2 cm/s were removed from all analysis. The

684   smoothed spikes number vector was divided by the smoothed occupancy time vector to

685   obtain the firing rate vector for each trial. The firing rate vectors were pooled for a specific

686   condition (e.g., Familiar Objects Track) and direction of the animal (e.g., back) to generate a

687   firing rate map. These pooled vectors were also averaged to provide the mean firing rate

688   vector, corresponding to the mean firing rate for each spatial bin.

689   **Pyramidal Cell Classification**

690   Cells with a mean firing rate lower than 20 Hz and either a burst index (Royer et al., 2012)

691   greater than 0 or the spike duration greater than 0.4 ms were classified as putative

692   pyramidal neurons. They were classified as interneurons otherwise.

693   **Active Cells Classification**

694   A cell was considered as active when the mean firing rate was greater than 0.5 Hz, the peak

695   firing rate was greater than 1.5 Hz and the cell fired at least one spike in 50% of the trials.

696   These 3 criteria had to be verified in either the forth or back direction.

697   **Place Fields Detection**

698   To detect a mean place field, a bootstrap procedure was performed. For each trial, a new

699   spikes train was generated using a Poisson process with λ equal to the mean firing rate of

700   the trial and a 1 ms time interval. A "randomized" firing rate map was then generated and

701   the mean firing rate vector was determined and compared with the mean firing rate vector

702   from the initial rate map. This operation was repeated 1000 times to determine a *P*-value

703   vector (*P*-value for each 2 cm spatial bin). Place fields candidates were defined as a set of

704   more than 3 continuous spatial bins associated with *P*-values lower than 0.01. Two place

705   fields were merged when the distance between their closest edges was at most equal to 5

706   spatial bins (10 cm). Place fields' edges were extended by at most 5 spatial bins (for each

707   edge) when the *P*-value was below 0.30 for these bins. A field with a size greater than 45

708   spatial bins (90 cm) was not considered as a place field. To validate a mean place field, the

709   cell had to verify a stability criterion. Spatial correlations were calculated between the firing

710   rate vector of each trial and the mean firing rate vector. The spatial bins corresponding to

711   other detected place fields were not considered in the spatial correlations. The place field

712   was validated if the spatial correlations were greater than 0.60 for at least 40% of trials.

713   Unless specified, when several mean place fields were detected, only the place field with the

714   highest peak was conserved. An active cell with at least one place field in one direction was

715   considered as a place cell.

716   The same procedure was applied to detect place fields per lap without the stability criterion,

717   which cannot be calculated on single trials. A place field per lap was conserved if it

718   overlapped at least 1 spatial bin with the closest mean place field.

719   **Stability Index**

720   The stability index of a cell was computed as the mean of the spatial correlations between all

721   pairs of firing rate vectors. This way, the cell stability index takes into account the activity

722   patterns from all the trials and provides a reliable quantification of the inter-trial

723   reproducibility of the cells activity. Note that this stability index is different from usual

724   stability indexes based on correlations of mean firing rates between even and odd trials or

725   two halves of the same recording session thus values obtained cannot be directly compared.

726   **Spatial Information**

727   The spatial information (SI) was calculated according to the following formula (Skaggs et al.,

728   1996):

$$SI = \sum_{i=1}^{N} \left[\frac{FR_i}{\overline{FR}} \times \frac{OT_i}{OT_T} \times log_2 \left(\frac{FR_i}{\overline{FR}} \right) \right]$$

729   where N is the number of spatial bins (N = 100), FR_i is the mean firing rate determined in

730   the i-th spatial bin, $\overline{FR}$ is the mean firing rate, OT_i is the mean occupancy time determined

731   in the i-th spatial bin, OT_T is the total occupancy time based on the mean occupancy time

732   vector.

26

733 As another measure of spatial information, we computed the Mutual Information using the

734 following formula:

$$MI = \sum_{i=1}^{N} \sum_{j=1}^{4} p_{i,j} log_2 \left(\frac{p_{i,j}}{p_i \cdot p_j} \right)$$

735 Where N is the total number of spatial bins, p_i is the occupancy probability of the animal in

736 the i-th spatial bin, p_j is the probability to obtain a firing rate amongst one of 4 non

737 overlapping quartiles of firing rates and $p_{i,j}$ is the joint probability of the animal to be in the i-

738 th spatial bin with a firing rate in the j-th quartile. The Mutual Information was then

739 normalized with a surrogate based distribution to correct possible bias due to basal firing

740 rate (Souza et al., 2018).

741 **Out/In Field Firing Ratio**

742 The out/in field firing ratio was computed as the ratio between the mean firing rate outside

743 the mean place field (excluding secondary place fields) and the mean firing rate inside the

744 mean place field.

745 **Place Field Dispersion**

746 A place field dispersion measure has been computed to quantify how much each place field

747 per lap was dispersed around the mean place field. The place field dispersion (PFD) was

748 calculated according to the following formula:

$$PFD = \frac{L}{N} \left[\frac{1}{M} \sum_{i=1}^{M} (C - C_i)^2 \right]^{\frac{1}{2}}$$

749 where C is the center of the mean place field, C_i is the center of the field in the i-th lap and M

750 is the number of laps with a single-trial detected field, L is the total length of the maze and N

751 is the number of spatial bins. The center of a place field was defined as the spatial bin with

752 the highest firing rate.

753 **Place Field Width**

754 Place field width was computed as the distance between the place field edges and only

755 determined for entire place fields. A place field was considered as complete when its firing

756 rate increased above 30% of the difference between highest and lowest place field activity

757 and then dropped below this threshold.

758 **On-Track and End-Track Fields**

759 A mean place field was considered as End-Track field if the peak of the field was located at

760 the beginning of the reward zone (i.e., at the 11-th or the 90-th spatial bin). All other fields

761 were classified as On-Track fields.

762 **Distribution of place fields' position**

763 To statistically assess whether the place fields were non-uniformly distributed in the maze,

764 we tested the null hypothesis that all fields were uniformly distributed. Based on this

765 hypothesis, the total number of place fields was redistributed with an equal probability to be

766 in each 10-cm spatial bin. The standard deviation of this uniform distribution was then

767 compared to the initial distribution. This operation was repeated 1000 times (bootstrap

768 procedure) to obtain a *P*-value, corresponding to the probability of the place fields to be

769 uniformly distributed. When this *P*-value was lower than 0.05, the null hypothesis was

770 rejected and the distribution was considered as non-uniform. To ensure that single values of

771 place fields' percentage in a given bin did not make the distribution non-uniform, values

772 greater than the 93-th percentile and lower than the 6-th percentile have been excluded

773 from the initial distribution.

774 **Local Stability**

775 A local stability index was developed to assess how consistent a firing rate was over the laps

776 for a given spatial bin. To this end, two mean firing rate vectors were calculated, in the

777 neighborhood of each spatial bin (2-spatial bins half-window) for even and odd trials. Local

778 stability index was defined as the spatial correlation between these two vectors for a given

779 spatial bin.

780 **Position Decoding**

781 To address how informative the firing rates of the CA1 pyramidal cells ensemble were about

782 the position of the animal in the different virtual environments, we used Bayesian decoding

783 and Firing Rate Vectors (FRV) methods. For each time window, the distribution of the animal

784 position probability across the whole maze was calculated using the firing activity of all

785 active cells (place cells and non place cells). The mode of this distribution (maximum of

786 probability) was chosen as the decoded position for a given time window. We used a

787 classical "memoryless" Bayesian decoder (Brown et al., 1998; Zhang et al., 1998). The

788 decoding of the spikes data was restricted to periods when the animal was running (speed >

789 2 cm/s) or with good Theta/Delta ratio and cross-validated using the "leave one out"

790   approach. We computed the animal's probability to be in each spatial bin *x* (2 cm) knowing

791   that N cells fired *n* spikes in a time window according to the following formula:

$$P(x|n) = C(\tau, \text{n})P(\text{x})\left(\prod_{i=1}^{N} f_i(x)^{n_i}\right)\exp\left(-\tau\sum_{i=1}^{N} f_i(x)\right)$$

792   with *P(x)* a uniform spatial prior, $f_i(x)$ the average firing rate of the neuron *i* over *x* (i.e., the

793   tuning curve over the position), n_i the number of spikes emitted by the neuron *i* in the

794   current time window and τ the length of the time window (150 ms; non-overlapping) and

795    $C(\tau, n)$ a normalization factor intended to set the posterior probability for one time window

796   to 1. This formula assumes that the spikes trains obey to a Poisson process and that cells

797   activity is independent. Position decoding was also preformed using the FRV method

798   (Middleton and McHugh, 2016). For each 100 ms time bin, the Pearson correlations were

799   calculated between firing rates across all cells and the mean firing rates from all cells for a

800   given spatial bin. A decoding error was defined as the absolute value of the difference

801   between decoded and real position. Accuracy was defined as the probability at the real

802   position in a particular time bin. To ensure that the position decoding was not influenced by

803   the number of cells, a drop cell approach was performed (van der Meer et al., 2010). Briefly,

804   for M recorded active cells, the position was decoded using k different subsets of cells with

805   increasing sizes 5*k with k ranging from 1 to the last multiple of 5 < M. For the k-th subset,

806   the decoding was repeated 50 times using 5*k randomly selected cells and the median value

807   of probabilities for a given time and spatial bin was chosen as the final probability. The

808   presented results were computed for a subset composed of 20 cells (k = 4).

809   **Map Similarity over Trials**

810   To analyze the dynamic of the changes of spatial representation between familiar and novel

811   conditions, map similarities were performed for 10 back and forth trials before and after the

812   experimental manipulation. For each active putative pyramidal cell, map similarities

813   consisted of the Pearson correlation between the firing rate map of each back and forth trial

814   and a template firing rate map. This template firing rate map was calculated as the average

815   of the firing rate map from all the laps in the condition with objects (most stable condition).

816   The maps corresponding to back (forth) trials were correlated to the mean back (forth) trial

817   map in the object condition and the correlations values were averaged to obtain a single

818   value for this back and forth trial. When map similarity was determined for a lap in the

819   object condition, the template firing rate map was computed without it.

29

Landmark Vector cells detection

For this analysis, we defined individual objects zones (IOZ) for each object. For a given object, IOZ corresponded to all spatial bins occupied by the object plus an additional margin of 7 spatial bins (14 cm), which was always located before the object in the animals' movement reference frame to take into account the anticipatory nature of some LV cells (Geiller et al., 2017). Thus IOZ for each object were different for back and forth directions. Here are the IOZ defined for each object in both directions: origami crane: 20-42 cm and 32-56 cm, cube: 46-68 cm and 60-82 cm and tree 154-180 cm and 166-180 cm. A cell was classified as LV cell if at least one of its place fields was in the same IOZ for both directions (note that secondary mean place fields were included in this analysis).

Phase precession Analysis

Phase precession was calculated on all spikes (above speed threshold) for the track with objects but restrained to Spatially Stable Trials (SST) in the no object condition to equalize stability between both conditions. SST consisted of at least 3 trials where the in-field correlation with the mean place field exceeded 0.6. To assess theta phase precession, the Local Field Potential (LFP) of the channel with the highest number of pyramidal cells (Skaggs et al., 1996) was filtered (4th order Chebyshev filter type II) in the theta band (4-12Hz). The instantaneous theta phase for each time bin (1 ms) was determined using the Hilbert transform of the filtered LFP and a phase was attributed to each spike. Only theta phase locked cells were considered in the following analysis (non-uniform phase distribution, $P < 0.05$, Rayleigh test). Circular linear analysis was used to determine the correlation strength and slope value of the relation between spikes phases and normalized positions (0-1) through the mean place field (Kempter et al., 2012). Briefly, the phase precession slope was computed with a linear regression model between circular (spike phases) and linear (animal's position) data. The slope of the regression was used to scale the animal's position and to transform it into a circular variable. A circular-circular correlation could thus be computed on the data to assess the strength of the relationship between spike phases and animal's position. A significance value was determined by re-computing the correlation values for 1000 permutations of the spikes position.

Analysis of phase precession on single-trial detected fields was also performed (Schmidt et al., 2009). Phase precession slope and correlation values were computed similarly to the previously described method. The single lap slope and correlation values were averaged

30

852   only for sessions with at least 3 significantly precessing trials where the cell emitted a

853   minimum of 4 spikes inside the mean place field.

854   **Unit-LFP shift and Spike Phase Spectrum**

855   To quantify phase precession independently of the position of the animal and the place field

856   detection, Unit-LFP shift was used. For all active putative pyramidal cells, a discreet

857   multitaper spectrum in the theta band (4-12Hz) of the cell's spikes was performed

858   (mtpointspectrum, Chronux) as well as the continuous multitaper spectrum of the

859   simultaneously recorded LFP (mtspectrumc, Chronux). A theta modulation index (Mizuseki et

860   al., 2009) was defined for each cell spike spectrum as the mean power around the peak

861   theta frequency ± 0.5 Hz divided by the mean power below 5Hz or above 9Hz. A cell was

862   considered as theta modulated if this index was greater than 1.4. The cross correlogram was

863   then calculated for theta modulated cells to determine the lag in the theta band between

864   the LFP and the cells' spectrum (Geisler et al., 2007). A positive lag indicates that the cell is

865   firing faster than the concurrent LFP.

866   **Speed modulation of theta frequency and Amplitude**

867   The instantaneous theta frequency was computed from the instantaneous theta phase

868   extracted from the Hilbert transform of the filtered LFP in the theta band. For each time t_i,

869   the instantaneous theta frequency ($F_\theta(t_i)$) was determined based on the unwrapped phase:

$$F_\theta(t_i) = \frac{Phase(t_{i+1}) - Phase(t_i)}{2\pi * Fs}$$

870   where *Fs* is the sampling frequency.

871   Instantaneous theta amplitude was defined as the module of the LFP Hilbert transform and

872   normalized by the mean LFP theta amplitude. The Pearson correlation coefficient was then

873   calculated between the speed of the animal and theta frequency/amplitude.

874   A theta peak detection method was also used to calculate the instantaneous theta

875   frequency. Theta peaks were detected with zero crossing of the instantaneous LFP phase

876   and frequency was deduced from the time between two successive theta peaks. This value

877   was affected to all the time stamp of the corresponding cycle.

878   **Theta timescale correlation**

879   To calculate the theta timescale lag between the spikes of two overlapping place fields, two

880   cross-correlograms (CCGs) were computed (Skaggs et al., 1996; Dragoi and Buzsáki, 2006;

881   Robbe and Buzsaki, 2009). First a "Real time-scale" CCG was computed with a 1 s time

31

882   window and 3 ms time bin. The CCG time lag was defined as the peak of the filtered CCG

883   between [0-2] Hz. "Theta time-scale" CCG was computed with a 200 ms time window and 1

884   ms time bin. The theta time lag was defined as the peak of the filtered CCG between [0-20]

885   Hz. Only pairs of cells with a CCG mean bin count of 1 count/ms were included in this

886   analysis. The relation between the CCG time lag and theta time lag was assessed using

887   Pearson correlation.

888   **Preferred Theta Phase**

889   Preferred theta phase and Mean Resultant Vector Length of each cell were defined thanks to

890   circ_mean and circ_r circular statistics Matlab toolbox functions (Berens, 2009). Global

891   phase 180° was defined as the maximal pyramidal cells activity (Skaggs et al., 1996).

892

893   **Code availability**

894   All custom written codes used in the present study are available upon reasonable request.

895   **Statistics**

896   All statistical analyses were conducted using Matlab codes (MathWorks). For each

897   distribution, a Lilliefors goodness-of-fit test was used to verify if the data were normally

898   distributed and a Levene test was used to assess for equal variance. If normality or equal

899   variance were not verified, we used the Wilcoxon rank sum test otherwise the Student t-test

900   was used to compare two distributions. In case of multiple comparisons, the Kruskal-Wallis

901   test with Bonferroni post-hoc test was used. Spatial correlations were computed using

902   Pearson's correlation coefficient. Chi-square test was used to compare percentages of phase

903   precessing cells. For circular distributions comparison, we first tested if they came from a

904   Von-Mises distributions (Watson Test) with a common concentration (circ_ktest), if the

905   distribution respected these constrains circular ANOVA: Watson-Williams multi-sample test

906   for equal means (circ_wwtest) was applied.

907

908   **Data availability**

909   Data acquired in the present work are stored on INMED server and available upon

910   reasonable request.

References

Aronov D, Tank DW (2014) Engagement of Neural Circuits Underlying 2D Spatial Navigation in a Rodent Virtual Reality System. Neuron 84:442–456.

Barry C, Lever C, Hayman R, Hartley T, Burton S, O'Keefe J, Jeffery K, Burgess N (2006) The Boundary Vector Cell Model of Place Cell Firing and Spatial Memory. Rev Neurosci 17:71–97.

Battaglia FP (2004) Local Sensory Cues and Place Cell Directionality: Additional Evidence of Prospective Coding in the Hippocampus. J Neurosci 24:4541–4550.

Berens P (2009) CircStat : A *MATLAB* Toolbox for Circular Statistics. J Stat Softw.

Brown EN, Frank LM, Tang D, Quirk MC, Wilson M a (1998) A statistical paradigm for neural spike train decoding applied to position prediction from ensemble firing patterns of rat hippocampal place cells. J Neurosci 18:7411–7425.

Burke SN, Maurer AP, Nematollahi S, Uprety AR, Wallace JL, Barnes CA (2011) The influence of objects on place field expression and size in distal hippocampal CA1. Hippocampus 21:783–801.

Cabral HO, Fouquet C, Rondi-Reig L, Pennartz CMA, Battaglia FP (2014) Single-Trial Properties of Place Cells in Control and CA1 NMDA Receptor Subunit 1-KO Mice. J Neurosci 34:15861–15869.

Chen G, King JA, Burgess N, O'Keefe J (2013) How vision and movement combine in the hippocampal place code. Proc Natl Acad Sci 110:378–383.

Cohen JD, Bolstad M, Lee AK (2017) Experience-dependent shaping of hippocampal CA1 intracellular activity in novel and familiar environments. Elife 6:1–27.

Connor CE, Knierim JJ (2017) Integration of objects and space in perception and memory. Nat Neurosci 20:1493-1503.

Danielson NB, Zaremba JD, Kaifosh P, Bowler J, Ladow M, Losonczy A (2016) Sublayer-Specific Coding Dynamics during Spatial Navigation and Learning in Hippocampal Area CA1. Neuron 91:652–665.

Deshmukh SS, Knierim JJ (2011) Representation of Non-Spatial and Spatial Information in the Lateral Entorhinal Cortex. Front Behav Neurosci 5:69.

Deshmukh SS, Knierim JJ (2013) Influence of local objects on hippocampal representations: Landmark vectors and memory. Hippocampus 23:253–267.

Dragoi G, Buzsáki G (2006) Temporal Encoding of Place Sequences by Hippocampal Cell Assemblies. Neuron 50:145-57.

957   Dupret D, O'Neill J, Pleydell-Bouverie B, Csicsvari J (2010) The reorganization and
958   reactivation of hippocampal maps predict spatial memory performance. Nat Neurosci
959   13:995–1002.
960

961   Epstein RA, Patai EZ, Julian JB, Spiers HJ (2017) The cognitive map in humans: Spatial
962   navigation and beyond. Nat Neurosci 20:1504–1513.
963

964   Fenton AA, Kao H-Y, Neymotin SA, Olypher A, Vayntrub Y, Lytton WW, Ludvig N (2008)
965   Unmasking the CA1 Ensemble Place Code by Exposures to Small and Large
966   Environments: More Place Cells and Multiple, Irregularly Arranged, and Expanded Place
967   Fields in the Larger Space. J Neurosci 28:11250–11262.
968

969   Geiller T, Fattahi M, Choi JS, Royer S (2017) Place cells are more strongly tied to landmarks in
970   deep than in superficial CA1. Nat Commun 8:14531.
971

972   Geisler C, Robbe D, Zugaro M, Sirota A, Buzsaki G (2007) Hippocampal place cell assemblies
973   are speed-controlled oscillators. Proc Natl Acad Sci U S A 104:8149–8154.
974

975   Geva-Sagiv M, Las L, Yovel Y, Ulanovsky N (2015) Spatial cognition in bats and rats: From
976   sensory acquisition to multiscale maps and navigation. Nat Rev Neurosci 16:94–108.
977

978   Hartley T, Burgess N, Lever C, Cacucci F, O'Keefe J (2000) Modeling place fields in terms of
979   the cortical inputs to the hippocampus. Hippocampus 10:369–379.
980

981   Hetherington PA, Shapiro ML (1997) Hippocampal place fields are altered by the removal of
982   single visual cues in a distance-dependent manner. Behav Neurosci 111:20–34.
983

984   Hirase H, Czurkó A, Csicsvari J, Buzsáki G (1999) Firing rate and theta-phase coding by
985   hippocampal pyramidal neurons during "space clamping." Eur J Neurosci 11:4373–4380.
986

987   Hollup S a, Molden S, Donnett JG, Moser MB, Moser EI (2001) Accumulation of hippocampal
988   place fields at the goal location in an annular watermaze task. J Neurosci 21:1635–1644.
989

990   Holscher C (2005) Rats are able to navigate in virtual environments. J Exp Biol 208:561–569.
991

992   Kempter R, Leibold C, Buzsáki G, Diba K, Schmidt R (2012) Quantifying circular-linear
993   associations: Hippocampal phase precession. J Neurosci Methods 207:113–124.
994

995   Kentros CG, Agnihotri NT, Streater S, Hawkins RD, Kandel ER (2004) Increased attention to
996   spatial context increases both place field stability and spatial memory. Neuron 42:283–
997   295.
998

999   Knierim JJ, Hamilton DA (2011) Framing spatial cognition: neural representations of proximal
1000   and distal frames of reference and their roles in navigation. Physiol Rev 91:1245–1279.
1001

1002   Knierim JJ, Neunuebel JP, Deshmukh SS (2013) Functional correlates of the lateral and
1003   medial entorhinal cortex: objects, path integration and local-global reference frames.

1004   Philos Trans R Soc B Biol Sci 369:20130369
1005
1006   Knierim JJ, Rao G (2003) Distal landmarks and hippocampal place cells: Effects of relative
1007   translation versus rotation. Hippocampus 13:604–617.
1008
1009   Le Merre P, Esmaeili V, Charrière E, Galan K, Salin PA, Petersen CCH, Crochet S (2018)
1010   Reward-Based Learning Drives Rapid Sensory Signals in Medial Prefrontal Cortex and
1011   Dorsal Hippocampus Necessary for Goal-Directed Behavior. Neuron 97:83–91.
1012
1013   McNaughton BL, Battaglia FP, Jensen O, Moser EI, Moser MB (2006) Path integration and the
1014   neural basis of the "cognitive map." Nat Rev Neurosci 7:663–678.
1015
1016   Middleton SJ, McHugh TJ (2016) Silencing CA3 disrupts temporal coding in the CA1
1017   ensemble. Nat Neurosci 19:945–951.
1018
1019   Mizuseki K, Sirota A, Pastalkova E, Buzsáki G (2009) Theta Oscillations Provide Temporal
1020   Windows for Local Circuit Computation in the Entorhinal-Hippocampal Loop. Neuron
1021   64:267–280.
1022
1023   Muller RU, Kubie JL, Ranck JB (1987) Spatial firing patterns of hippocampal complex-spike
1024   cells in a fixed environment. J Neurosci 7:1935–1950.
1025
1026   O' Keefe J, Burgess N (1996) Geometric determinants of the place fields of hippocampal
1027   neurons. Nature 381:425–428.
1028
1029   O'Keefe J, Conway DH (1978) Hippocampal place units in the freely moving rat: why they fire
1030   where they fire. Exp Brain Res 31:573–590.
1031
1032   O'Keefe J, Nadel L (1978) The hippocampus as a cognitive map. hippocampus as a Cognitive
1033   map. (Oxford University Press, London).
1034
1035   O'Keefe J, Recce ML (1993) Phase relationship between hippocampal place units and the EEG
1036   theta rhythm. Hippocampus 3:317–330.
1037
1038   Poucet B, Chaillan F, Truchet B, Save E, Sargolini F, Hok V (2015) Is there a pilot in the brain?
1039   Contribution of the self-positioning system to spatial navigation. Front Behav Neurosci
1040   9:1–10.
1041
1042   Ravassard P, Kees A, Willers B, Ho D, Aharoni D, Cushman J, Aghajan ZM, Mehta MR (2013)
1043   Multisensory control of hippocampal spatiotemporal selectivity. Science 340:1342–
1044   1346.
1045
1046   Renaudineau S, Poucet B, Save E (2007) Flexible use of proximal objects and distal cues by
1047   hippocampal place cells. Hippocampus 17:381–395.
1048
1049   Rich PD, Liaw HP, Lee AK (2014) Large environments reveal the statistical structure governing
1050   hippocampal representations. Science 345:814–817.

1051

1052   Robbe D, Buzsaki G (2009) Alteration of Theta Timescale Dynamics of Hippocampal Place
1053   Cells by a Cannabinoid Is Associated with Memory Impairment. J Neurosci
1054   29(40):12597-605.

1055

1056   Rossant C, Kadir SN, Goodman DFM, Schulman J, Hunter MLD, Saleem AB, Grosmark A,
1057   Belluscio M, Denfield GH, Ecker AS, Tolias AS, Solomon S, Buzski G, Carandini M, Harris
1058   KD (2016) Spike sorting for large, dense electrode arrays. Nat Neurosci 19:634–641.

1059

1060   Royer S, Zemelman B V., Losonczy A, Kim J, Chance F, Magee JC, Buzsáki G (2012) Control of
1061   timing, rate and bursts of hippocampal place cells by dendritic and somatic inhibition.
1062   Nat Neurosci 15:769–775.

1063

1064   Sato M, Mizuta K, Islam T, Kawano M, Gomez-Dominguez D, Kim K, Yamakawa H, Ohkura M,
1065   Fukai T, Nakai J, Hayashi Y (2018) Dynamic embedding of salience coding in
1066   hippocampal spatial maps. bioRxiv:1–74.

1067

1068   Schlesiger MI, Cannova CC, Boublil BL, Hales JB, Mankin EA, Brandon MP, Leutgeb JK, Leibold
1069   C, Leutgeb S (2015) The medial entorhinal cortex is necessary for temporal organization
1070   of hippocampal neuronal activity. Nat Neurosci 18:1123–1132.

1071

1072   Schmidt R, Diba K, Leibold C, Schmitz D, Buzsaki G, Kempter R (2009) Single-Trial Phase
1073   Precession in the Hippocampus. J Neurosci 29:13232–13241.

1074

1075   Sheynikhovich D, Chavarriaga R, Strösslin T, Arleo A, Gerstner W (2009) Is There a Geometric
1076   Module for Spatial Orientation? Insights From a Rodent Navigation Model. Psychol Rev
1077   116:540–566.

1078

1079   Skaggs WE, McNaughton BL, Wilson MA, Barnes CA (1996) Theta phase precession in
1080   hippocampal neuronal populations and the compression of temporal sequences.
1081   Hippocampus 6:149–172.

1082

1083   Souza BC, Pavão R, Belchior H, Tort ABL (2018) On Information Metrics for Spatial Coding.
1084   Neuroscience. 375:62-73.

1085

1086   Spiers HJ, Hayman RMA, Jovalekic A, Marozzi E, Jeffery KJ (2015) Place field repetition and
1087   purely local remapping in a multicompartment environment. Cereb Cortex 25:10–25.

1088

1089   Strösslin T, Sheynikhovich D, Chavarriaga R, Gerstner W (2005) Robust self-localisation and
1090   navigation based on hippocampal place cells. Neural Networks 18:1125–1140.

1091

1092   Taylor KD (1978) Range of Movement and Activity of Common Rats (Rattus Norvegicus) on
1093   Agricultural. J Appl Ecol 15:663–677.

1094

1095   Tolman EC (1948) Cognitive maps in rats and men. Psychol Rev 55:189–208.

1096

1097   van der Meer MAA, Johnson A, Schmitzer-Torbert NC, Redish AD (2010) Triple dissociation of

1098   information processing in dorsal striatum, ventral striatum, and hippocampus on a
1099   learned spatial decision task. Neuron 67:25–32.
1100

1101   Wiener SI, Paul CA, Eichenbaum HB (1989) Spatial and behavioral correlates of hippocampal
1102   neuronal activity. J Neurosci 9:2737–2763.
1103

1104   William E. Skaggs and Bruce L. McNaughton and Katalin M. Gothard and Etan J. Markus
1105   (1993) An Information-Theoretic Approach to Deciphering the Hippocampal Code. Proc
1106   IEEE:1030–-1037.
1107

1108   Wilson M, McNaughton B (1993) Dynamics of the hippocampal ensemble code for space.
1109   Science (80-) 261:1055–1058.
1110

1111   Youngstrom IA, Strowbridge BW (2012) Visual landmarks facilitate rodent spatial navigation
1112   in virtual reality environments. Learn Mem 19:84–90.
1113

1114   Zhang K, Ginzburg I, McNaughton BL, Sejnowski TJ (1998) Interpreting neuronal population
1115   activity by reconstruction: unified framework with application to hippocampal place
1116   cells. J Neurophysiol 79:1017–1044.
1117

A
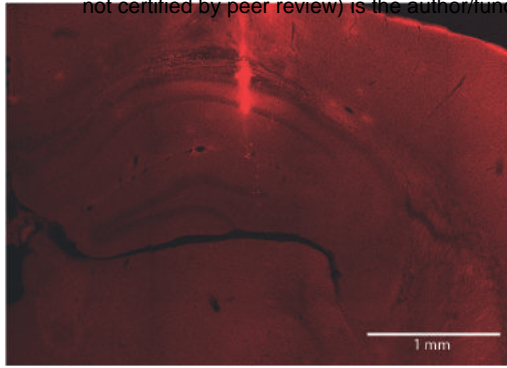
B
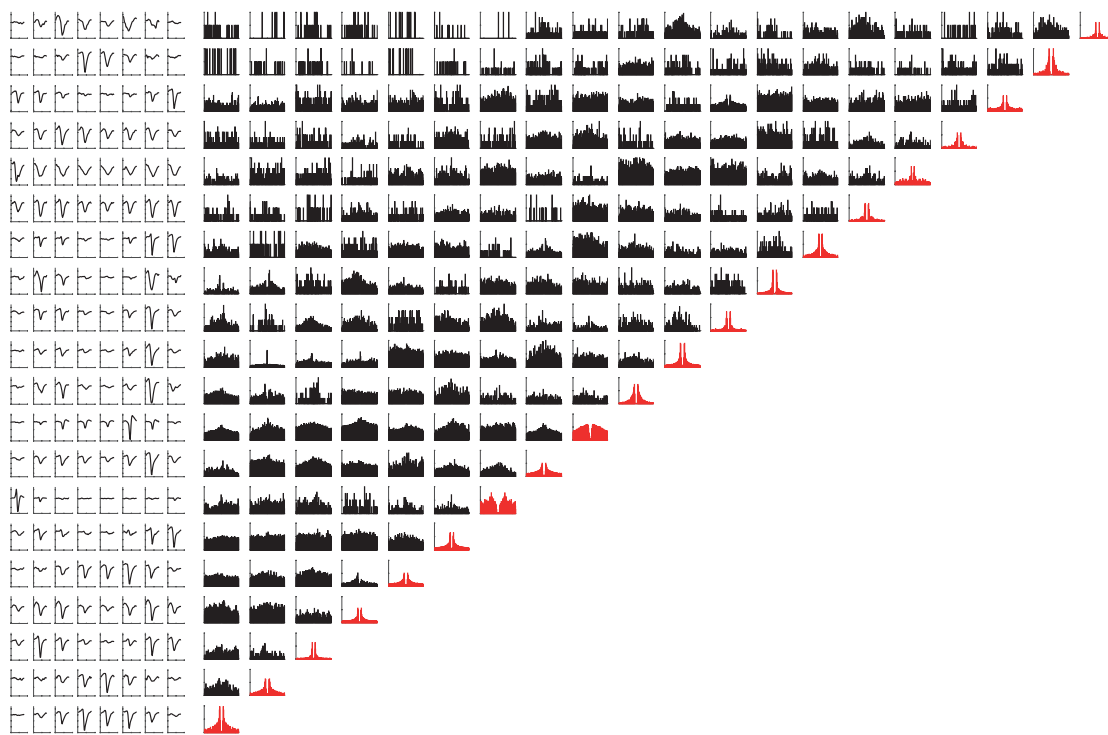
Figure 1 - figure supplement 1: Histology and spike sorting

A. Representative histology slide showing a silicon probe track ending in CA1 pyramidal layer. Scale bar: 1mm. **B.** (Right) Auto-correlograms (red) and cross-correlograms (black) of 20 CA1 units recorded simultaneously. (Left) Average units waveforms (for visualization each row is normalized by the unit maximum average waveform).
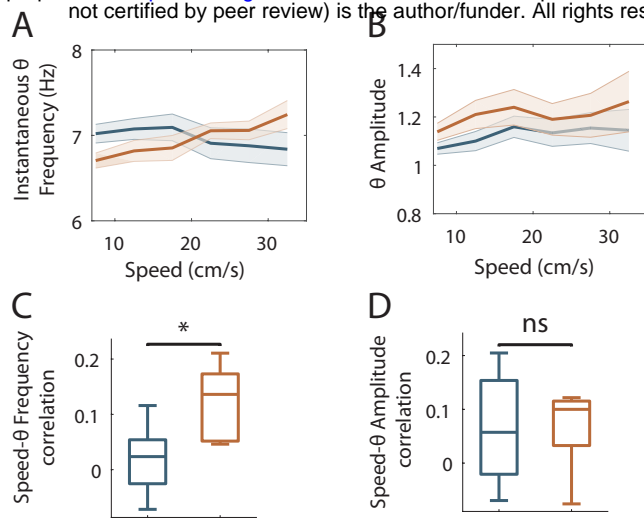
Figure 6 - figure supplement 1: Speed modulation of LFP theta frequency and amplitude in OT and ØT

 A-B. Mean theta frequency (**A**) or amplitude (**B**) across all recording sessions as a function of animal speed (bin: 5 cm/s). **C-D.** Box plots of the correlation between theta frequency (**C**; $P = 0.01$, two-tailed unpaired t-test) or amplitude (**D**; $P = 0.9$, two-tailed unpaired t-test) vs speed for individual sessions.
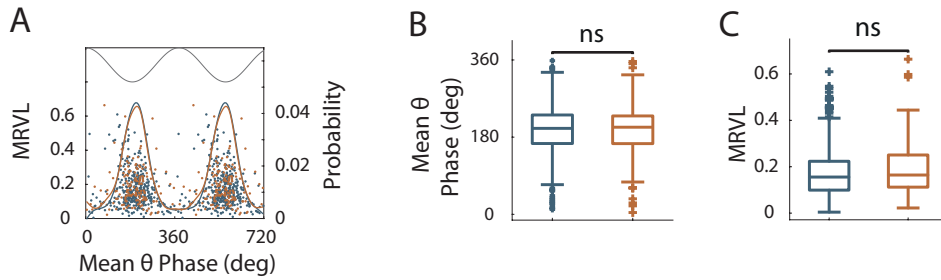
Figure 6 - figure supplement 2: Theta modulation of spikes in OT and ØT

A. Mean theta phase plotted against strength of phase locking (Mean Resultant Vector Length: MRLV) for all theta modulated cells ($P < 0.05$, Rayleigh Test) in OT (orange) and ØT (blue). Solid lines: probability distribution of the preferred theta phase for the two conditions. Black line: illustrative theta cycle **B.** Box plots of the mean theta phase for OT(orange) and ØT (blue) conditions ($P = 0.77$, F $= 0.08$, circular ANOVA) **C.** Box plots of the Mean Resultant Vector Length in OT(orange) and ØT (blue) conditions ($P = 0.1$, two-tailed WRS test).